NTNU
Norwegian University of
Science and Technology

Actuation moments for hydrofoil flaps

Ingvild Dagestad

NTNU Trondheim
Norwegian University of Science and Technology
Department of Marine Technology

MASTER THESIS IN MARINE TECHNOLOGY

SPRING 2018

FOR

Ingvild Dagestad

Actuation moments for hydrofoil flaps

A completely submerged hydrofoil system is unstable in both heave and roll. Active control of the hydrodynamic forces acting on the hydrofoil is therefore necessary in order to maintain a stable flight. This can be done by using a control algorithm that sets the position of flaps that are integrated into the hydrofoil design. In order to move the flaps, some type of actuator is necessary. For instance, this could be hydraulic cylinders or electric servo motors. The actuators must be strong enough to move the flap in all operating conditions. That is, they need to be able to generate a torque on the flap axel that is larger than any moment that can come from the flap. At the same time, the actuators should not be over-dimensioned, in order to save space and costs.

The objective of the master thesis is to investigate the necessary torque capacity of flap-actuators for a hydrofoil vessel, and the following sub-topics shall be covered

- Use CFD to calculate the hydrodynamic flap-moment on typical foil geometries

- Use simplified tools and methods – such as XFoil and equations found in the literature – to calculate the flap-moment and compare the results from these simplified methods to the results from CFD.

- Use the results to determine the required flap actuator torque capacity in a suitable case study

- Investigate the time dependence of the flap-moment

In the thesis the candidate shall present her personal contribution to the resolution of problem within the scope of the thesis work.

Theories and conclusions shall be based on mathematical derivations and/or logic reasoning identifying the various steps in the deduction.

The thesis work shall be based on the current state of knowledge in the field of study. The current state of knowledge shall be established through a thorough literature study, the results of this study shall be written into the thesis. The candidate should utilize the existing possibilities for obtaining relevant literature.

The thesis shall be organized in a rational manner to give a clear exposition of results, assessments, and conclusions. The text should be brief and to the point, with a clear language. Telegraphic language should be avoided.

NTNU Trondheim
Norwegian University of Science and Technology
Department of Marine Technology

The thesis shall contain the following elements: A text defining the scope, preface, list of contents, summary, main body of thesis, conclusions with recommendations for further work, list of symbols and acronyms, reference and (optional) appendices. All figures, tables and equations shall be numerated.

The supervisor may require that the candidate, in an early stage of the work, present a written plan for the completion of the work. The plan shall include a budget for the use of laboratory or other resources that will be charged to the department. Overruns shall be reported to the supervisor.

The original contribution of the candidate and material taken from other sources shall be clearly defined. Work from other sources shall be properly referenced using an acknowledged referencing system.

The thesis shall be submitted electronically (pdf) in DAIM:
- Signed by the candidate
- The text defining the scope (this text) (signed by the supervisor) included
- Computer code, input files, videos and other electronic appendages can be uploaded in a zip-file in DAIM. Any electronic appendages shall be listed in the main thesis.

The candidate will receive a printed copy of the thesis.

Supervisor   : Professor Sverre Steen
Co-supervisor   : Jarle Andre Kramer
Start   : 15.01.2018
Deadline   : 15.06.2018

Trondheim, 15.06.2018

Sverre Steen
Supervisor

Summary

The following thesis investigates how the computer software STAR-CCM+ and Xfoil are used to determine the hydrodynamic loads on the two foil profiles EP-PLER E817 and NASA/LANGLEY LS(1)-0417 (GA(W)-1) with trailing edge flaps. The foils are analysed with flap lengths of 0.1c, 0.25c and 0.4c, at a Reynolds number of $20 \cdot 10^6$, where c is the total foil chord length. STAR-CCM+ uses steady analysis performed with steady and unsteady solvers depending on when flow separation occurs for the different cases. The flap is deflected to increase lift, within the interval $0°$ to $20°$ or $22°$ with interval of $2°$. The main objective is to determine the design parameters for a hydraulic actuator. Hence, the focus is to determine the hinge moment generated by the hydrofoil. The thesis suggests one recommended actuator for each of the two foil profiles. From the CFD analysis a critical hinge moment of 225kNm is found for the EPPLER E817 profile with a flap length of 0.25c and a span of 4meter, at a Reynolds number of $20 \cdot 10^6$. For the NASA/LANGLEY LS(1)-0417 profile with a flap length of 0.1c and a span of 4meter, the critical hinge moment was found to be 5732Nm at a Reynolds number of $20 \cdot 10^6$. For the EPPLER E18 profile an actuator with piston diameter of 160mm and rod diameter of 80mm with a design pressure of 250 bar is recommended. For the NASA/LANGLEY LS(1)-0417 (GA(W)-1) an actuator with a piston diameter of 80mm and a rod diameter of 40mm with a design pressure of 250 bar is found to be sufficient.

Sammendrag

Denne masteroppgaven undersøker hvordan dataprogrammene STAR-CCM+ og Xfoil kan brukes for å fastsette de hydrodynamiske kreftene på to foilprofiler: EPPLER E817 og NASA/LANGLEY LS(1)-0417 (GA(W)-1), med klaff på følgende kant. Disse foilene blir analysert med klafflengder på 0.1c, 0.25c og 0.4c, ved Reynolds tall $20 \cdot 10^6$, hvor c er den totale kordlengden til foilen. STAR-CCM+ brukes til å beregne statiske situasjoner ved hjelp av tidsuavhengige og tidsavhengige løsere, valg av løser varierer med når seperasjon oppstår. Klaffen blir bøyd for å øke løft, dette blir gjort for intervallet $0°$ til $20°$ eller $22°$ med intervall på $2°$. Hovedformålet med oppgaven er å bestemme designparametere for en hydraulisk aktuator. Derfor er hovedfokuset å finne momentet på klaffhengselen generert av hydrofoilen. Oppgaven foreslår en anbefalt aktuator for hver av foilprofilene. Fra CFD-analysene ble et kritisk moment på 225kNm estimert for EPPLER E817-profilen med en klafflengde på 0.25c og en bredde på 4 meter ved Reynoldstall $20 \cdot 10^6$. For NASA/LANGLEY LS(1)-0417-profilen med en klafflengde på 0.1c og en bredde på 4 meter, ble det kritiske momentet fastsatt til 5732Nm ved et Reynoldstall på $20 \cdot 10^6$. For EPPLER E817-profilen ble an aktuator med stempeldiameter på 160mm og en stempelstagdiameter på 80mm ved designtrykk på 250bar anbefalt. For NASA/LANGLEY LS(1)-0417 (GA(W)-1)-profilen ble en aktuator med stempeldiameter på 80mm og stempelstagdiameter på 40mm ved designtrykk på 250bar funnet passende.

Preface

This thesis is the concluding work of a 5-year Master of Science degree at the department of Marine Technology at NTNU Trondheim. I would like to thank my supervisor Sverre Steen for seeing the value of this study. I would also like to thank my co-supervisor Jarle Vinje Kramer for guiding me through this thesis and finding time for our weekly meetings in his busy schedule. Finally, I must thank Jens P Høvik for all the nutritious dinners he has provided the last 5 years, keeping up my spirit and keeping me well fed.

Contents

List of Figures

List of Tables

Nomenclature

A	planform area of a foil, or efficient section of a piston
a_{actuator}	distance between flap hinge and actuator arm
B	turbulent wall-law intercept constant, ≈ 5
C_D	drag coefficient
C_F	friction coefficient
C_L	lift coefficient
C_p	pressure coefficient
c	chord length
c_f	flap length
D	drag force
Fn	Froud number, $\frac{U}{\sqrt{gL}}$
F_i	force in i direction
F_c	cylinder force
$\vec{f}$	body force per unit volume
g	gravitational acceleration
k	turbulent kinetic energy
L	characteristic length or lift force
n	surface normal
$\vec{P}$	surface force per unit volume
P_d	design pressure
$\tilde{P}_k$	turbulent kinetic energy production rate
p	pressure
Re	Reynolds number, $\frac{UL}{\nu}$
S	foil surface area
S_{cylinder}	cylinder stroke
s	hydrofoil span
s_f	flap span
t	foil thickness or time

U	inflow velocity or free stream velocity
$U_{induced}$	induced velocity
U_∞	free stream velocity
u_τ	friction velocity
$\bar{u}$	time mean velocity
$\vec{u}$	velocity vector field
y	distance from wall or y-coordinate
y^+	dimensionless distance from wall
α	angle of attack
α_f	flap angle
δ	boundary layer thickness
δ_{ij}	Kronecker-delta
ε	turbulence dissipation rate
$\dot{\varepsilon}$	strain-rate tensor
Γ	circulation
γ	local circulation distribution
κ	Karman constant, ≈ 0.41
μ	dynamic viscosity
ν	kinematic viscosity
ω	specific eddy dissipation rate
ρ	density

Acronyms

CAD	Computer-aided design
CFD	Computational fluid dynamics
CFL	Courant-Friedrichs-Lewy
FVM	Finite Volume Method
N-S	Navier-Stokes
RANS	Reynolds-averaged Navier-Stokes
SIMPLE	Semi-Implicit Method for Pressure-Linked Equations
SES	Surface effect ship
SST	Shear stress transport
SWAT	Small water plane area twin hull

1   Introduction

1.1   Background

High speed vessels have always been of interest in the marine field, particularly between the 1950's to the 1970's. Many theories for estimating the hydrodynamic loads have been developed and good agreement with experimental data has been found. Uncertainties are still present, however, and some rough estimates are necessary in the analysis and design of such crafts. Faltinsen [13] mentions SWAT, planing vessel, SES or air-cushion catamaran and hydrofoil vessel as the main high-speed vessels. The definition of what makes a craft highspeed is up for discussion. Two commonly used definitions for vessels supported by a submerged hull are:

- The operational speed is 30 knots, or

- The froude number (Fn) is above 0.4, where $Fn = U/\sqrt{Lg}$.

High-speed vessels are not always supported by a submerged hull, it is common do differ between displacement, semi-displacement and planing vessels, where the dominating forces will differ for each kind. For a semi-displacement vessel, the buoyancy force is not the dominating at full speed, as it is for a displacement vessel. The highspeed vessels are carried by a pressure that can be divided into hydrostatic and hydrodynamic pressure, where the speed or Froud number determines which one is dominating.

Hydrofoil vessels are supported by hydrofoils, the other high-speed vessels are supported either by the hull, air cushions or a combination. Hydrofoil crafts generally have good seakeeping behaviour in foilborne condition, and this makes them appropriate for different uses such as ferries and sailboats. In addition, they have quite low resistance as their hull is lifted out of the water, limiting the resistance to the foil system and the air resistance of the vessel. Some important parameters during design of such a vessel are: roll stability, directional stability and maintaining good stability when the hull is lifted out of the water. Safety is a big concern as always when designing offshore vessels, so good performance in rough seas is also important[13].

Cavitation and ventilation are also major issues when designing a hydrofoil vessel. As the operation speed is high, cavitation can easily occur and dramatically reduce the lift and it may also damage the foils. Ventilation is when an air pocket connected to the atmosphere appears at the suction side of the foils or struts, this air

pocket will reduce the lift on the foils. This can be fatal for the hydrofoil vessel as it may lead it to fall from flying condition, into the water at high speeds. This can cause both structural damage, as well as causing injuries to passengers. Cavitation occurs when the pressure at any point on the suction side of the hydrofoil becomes equal to the vapor pressure. It is possible to design a supercavitating foil where the suction side is not wetted, these usually have a lower lift coefficient than regular subcavitating foils[13]. Cavitation is not considered in this report but must always be kept in mind when designing hydrofoils and hydrofoil vessels, as it is usually the limiting factor for the possible maximum speed.

The foil system on hydrofoil vessels can be fully submerged or surface piercing, each have their advantages and disadvantages. Surface piercing systems are self-stabilising due to the change in wetted area caused by the different motions of the craft. E.g. is the roll motion of a ship where the wetted area at a given roll angel will increase on one side and decrease on the other. This results in a counteracting roll force that will stabilise the vessel[13]. This is not the case for fully submerged foil systems where an active control system is necessary. Flaps are often used on fully submerged foil systems to stabilise the vessel while manoeuvring and to maintain sufficient lift at different speeds. Such an active control system uses sensors to monitor the vessel attitude and change the flap angle to limit the position changes of the hydrofoil vessel. In order to control the flap angle an actuator can be used to hold the flap in the desired position, and it is usually mounted on the pressure side of the foil. The use of flaps on foils are very common in aeronautics, where the control mechanism is located within the air foil. This is possible because the dimensions on aircrafts are often larger than on hydrofoil vessels and the operation in air allows for finer mechanisms. Because the hydraulic arm is placed underneath the foil it is desired to make it as small as possible as it will disturb the flow field. Most importantly, however, the actuator must be strong enough to withstand the moment caused by the pressure difference over the foil.

1.2   Objectives

The general goal of this thesis is to find the parameters for an appropriate actuator to control the flaps on a fully submerged hydrofoil system. The main focus is on testing different methods for obtaining information about the hydrodynamic loads on the hydrofoil. The CFD software STAR-CCM+ is applied, in addition simpler tools are used and compared to the CFD results. This is to investigate the possibility of obtaining accurate analyses by simpler methods. This is useful

2

as enabling this would save both time and expenses.

1.3   Motivation

In order to recommend an appropriate actuator, it is necessary to investigate the hydrodynamic forces on the hydrofoils. This can be done using computational fluid dynamics (CFD). As for any tool it is important to apply it properly, and within its limitations. The author is not yet very familiar with the application of CFD software and will use this opportunity to gain knowledge about the theory and possibilities found within computational fluid dynamics. Another aspect of interest is the possibility of using more simple tools for obtaining information about hydrodynamic forces affecting bodies in a fluid flow. Xfoil for example is based on potential theory and uses panel method together with boundary layer theory to calculate the flow around air foils. This is a well-recognised software with regards to finding forces such as lift and drag on foils. If such software is sufficient for the purposes at hand, it would greatly simplify the work process while simultaneously reducing costs.

1.4   Scope and limitations

The hydrofoil system is assumed to have a span of 10 meters consisting of two flapped hydrofoils with span of 5 meters each and a chord length of 1 meter and the operational speed is assumed to be approximately 35 knots. As model testing is expensive and comprehensive, the force estimations will be completed in a CFD software called *STAR-CCM+*. The main limitations in CFD calculations are the computational resources and the available time. It is therefore necessary to achieve at a good setup with appropriate parameters to complete the necessary calculations at a reasonable time. The results obtained in this CFD software are also compared to the results found using Xfoil. Xfoil is an open source program developed at MIT in 1986 by Mark Drela[9] and it applies potential theory and boundary layer theory to calculate the flow around subsonic air foils. The application of this software is less time consuming and it would be convenient if this software could be applied instead of complex CFD analysis.

In this report the theories which the numerical calculations are based on are presented. This clarifies the basis and limitations of such methods which are important to keep in mind when evaluating the results obtained by the CFD software. As numerical calculations are resource demanding it is considered sufficient to conduct the analysis in 2D when the main goal is to find an appropriate actuator. This

is because the 2D analysis will give too much lift on the foil, which again results in a conservative estimation of the moment affecting the flap hinge. The foil will be fully submerged in an infinite fluid, this means that no free surface effects are included. Turbulent flow is incorporated in the calculations using turbulence modelling, hence boundary layer theory is included as a part of the literature study. This is a very complex subject so only the areas considered necessary to clarify the CFD analyses done in this report are presented. In addition, foil theory, potential theory and the panel method is briefly introduced as this is the basis for Xfoil and gives a brief understanding of how hydrofoils work.
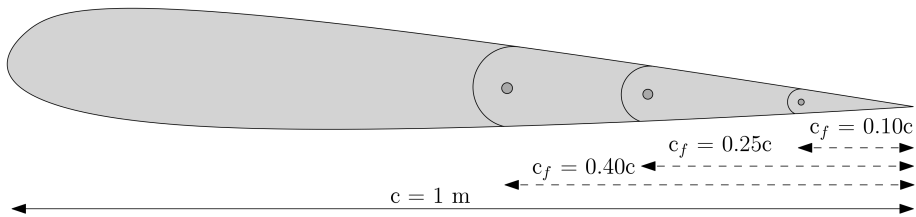
Figure 1: Foil with different flap sizes

The foil geometries analysed are first solidified using a computer aided design (CAD) program before they are imported into STAR-CCM+. Here a domain and grid independency study are conducted to ensure reliable results from the software calculations. The geometries tested are the EPPLER E817 and the NASA/LANGLEY LS(1)-0417, each with the flap sizes of 0.1c, 0.25c and 0.4c as demonstrated in figure 1. The geometries for both profiles can be seen in Appendix A. The lift, drag and moment coefficient is found for flap angles between 0 and 20-22 degrees (depending on the foil geometry) at a Reynolds number of 20 $\cdot 10^6$, this corresponds to a flow velocity of approximately 35 knots for the chord length tested. The numerical calculations are conducted either steady or unsteady. For small flap angles the flow will separate at or very close to the trailing edge, giving a steady flow problem with a constant lift. At larger flap angles separation will occur some distance before the trailing edge, resulting in an unsteady flow calling for the necessity of an unsteady solver.

Calculating the maximum moment that the flap hinge will be exposed to gives a good foundation for recommending a proper actuator for the hydrofoil vessel.

The 2D effects calculated will be made three dimensional without concern for the 3D effects acting on a 3D hydrofoil. This will give a conservative result making sure the actuator will be strong enough to hold the flap in the desired angle under any circumstances. The results obtained from the STAR-CCM+ analysis is discussed before an actuator is recommended. The general parameters applied in this study are listed in the table below.

Table 1: General parameters

c	1 m
c_f	0.1c, 0.25c and 0.4c
s	2x5 m
s_f	2x4 m
ρ	997.561 kg/m^3
ν	8.8871$\cdot$10^{-4} Pa$\cdot$s
$a_{actuator}$	5 -10 cm
U	17.8 m/s
Re	$\approx 20 \cdot 10^6$

1.5   Thesis structure

This report is structured into 9 sections as follows:

- Section 2: A short literature study on airfoil theory and the use of CFD software in previous studies is presented.

- Section 3: In this section a short background theory for CFD software, Xfoil and foil theory will be presented.

- Section 4: A presentation of the CFD software STAR-CCM+ and a description of the application of the program.

- Section 5: Here the independency study with regards to mesh and time is presented.

- Section 6: This section gives a brief description of the software Xfoil and how it is applied.

- Section 7: In this section the results obtained through the analyses are presented and discussed.

- Section 8: First the basic theory of a hydraulic cylinder is presented, before a cylinder is recommended for the cases studied.

- Section 9: A short conclusion of the work done is presented.

- Section 10: Finally, recommendations for further work is given.

2   Literature

When hydrofoils with flaps became a topic of interest in ship design, many foil profiles were tested and applied. The NACA-16 series were developed with hydrofoils in mind, but it turned out these had an unfortunate pressure distribution with regards to the use of flaps. This gave them low flap effectiveness[30]. This lead designers away from this profile, and many other profiles have been developed with great success. Flaps are widely used on airfoils and much research is completed in this area and can potentially be used in the future development of flaps on hydrofoils. The main differences between airfoils and hydrofoils are the medium in which they operate, this means that in hydrofoil design one will encounter issues such as cavitation and ventilation.

The effect of adding a flap to an airfoil is well known and described in many books including *Fundamentals of Aerodynamics*[21]. In aerodynamics there are several types of flaps, even slats which are flaps at the leading edge of the airfoil. A trailing edge flap is when the last portion of the trailing-edge is hinged to the rest of the body and common notation is that a downward deflection is a positive flap angle. Deflecting the flap downwards will give an increased lift coefficient due to the effective increase in the camber of the foil[21]. Flaps are effective to increase the maximum lift of a foil because if they are properly designed, separation can be delayed compared to the use of angle of attack, this is good for limiting drag[19]. Until the recent development within computer science it could be difficult to predict the hinge moment on a flapped wing section. Potential theory could be used but would give poor results as viscous effects greatly influences the flow at the aft of the foil[21].

In Hoerners book *Fluid-Dynamic Lift: Practical Information on Aerodynamic and Hydrodynamic lift*[19] it is found that after $\alpha_f = 60°$ there is only a small increase in the lift coefficient when the flap angle is increased. Considering the performance of flaps on airfoils the increase of angle of attack will reduce the effect of the flap. This will also be the case if the basic lift coefficient is increased in any other way. It should also be noted that the lift coefficient will increase with increasing c_f/c ratio but this also affects the drag negatively. In the aircraft industry a flap length of 20% of the chord length have proven most economical[19].

Choosing the right tool for analysing a foil is important, different methods have different weaknesses and uncertainties. Flow around air foils can be found by ex-

periments, for example in wind tunnels or by applying computer programs such as CFD softwares. Xfoil is a user-friendly free software developed by Mark Drela, it applies panel method and a coupled boundary layer integral method for analysing flow around subsonic 2D air foils. Tests show that the analysis are quite accurate compared to experimental results[15].

CFD software is not only used instead of experiments, it can also effectively complement experimental studies. In a study of a tidal turbine using hydrofoils with tubercles at the leading edge, STAR-CCM+ was used to obtain insight into the detailed flow[31]. The experiment was conducted in a cavitation tank with Reynolds number between $3{\cdot}10^5$ and $6{\cdot}10^5$ and the parameters of main interest were the lift and drag. The hydrofoils were then modelled in STAR-CCM+ and analysis were run. The force characteristics were similar, except for the drag coefficient which had a difference of about 10%. This large difference was most likely due to the uncertainty associated with the friction coefficient for the material used to make the tubercles. The visualisation capabilities of STAR-CCM+ then allowed for more detailed study of the flow around the foil and tubercles. This shows that CFD software can be a reliable and useful tool for fluid flow examination.

3   Theory

3.1   Foil theory

An asymmetric foil in a stream will have a suction and a pressure side. At the suction side the pressure will be lower than the static pressure, and the pressure on the pressure side will be higher than the static pressure. This leads to the foil being drawn towards the suction side resulting in a force called lift. Lift is generated on a foil in a flow if the foil is cambered or at an angle to the flow and is defined as the force working in the normal direction of the flow. The magnitude of the lift will depend on the angle of attack, the thickness, the camber and the flap angle of the hydrofoil. In addition to the lift force there will be a drag force that works in the flow direction, this is mostly due to viscous effects[13]. Drag due to viscous pressure may occur if vortex generation or separation is present[37]. The main characteristics of a 2D foil and its associated forces can be seen in figures 2 and 3.
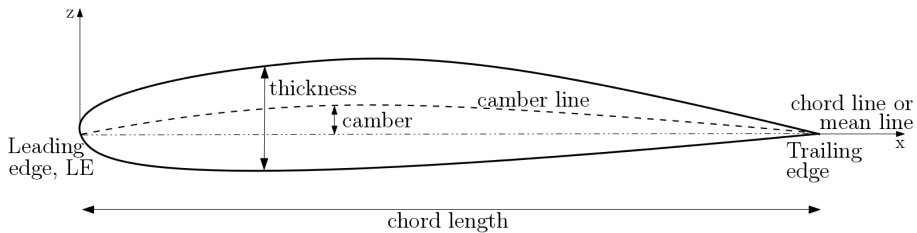

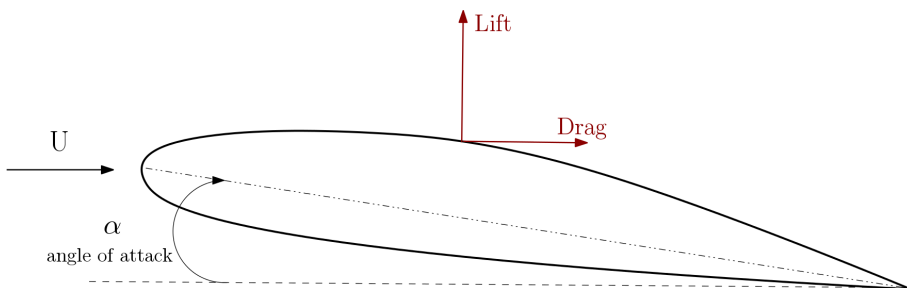Figure 2: 2D foil geometry definitions

Figure 3: 2D foil with angle of attack

To be able to compare and analyse the effectiveness of foils it is convenient to use dimensionless coefficients. The nondimensional drag and lift coefficient C_D and C_L are defined in equation 1, where A is the planform area of a foil. If a 2D foil is considered the A is replaced by the chord length, and when a moment is made dimensionless the A is replaced with c^2. The lift force F_L and drag force F_D can be found by equation 2[13], where p is the pressure, n is the surface normal and i is the force direction. Knowledge about the pressure distribution is not always readily available so other methods are often used to find the lift and drag force. As mentioned the main contribution to the drag is caused by viscosity and this drag can be estimated as in equation 3[18], where C_F is the friction coefficient for a smooth surface hull as given by the ITTC'57[37].

$$C_L = \frac{L}{0.5\rho U^2 A} \qquad\qquad C_D = \frac{D}{0.5\rho U^2 A} \tag{1}$$

$$F_i = -\int_S p n_i dS \tag{2}$$

$$C_D = 2C_F[1 + 2(t/c) + 60(t/c)^4] \qquad\qquad C_F = \frac{0.075}{(log_{10}Re - 2)^2} \tag{3}$$

In linear foil theory the velocity and pressure near the foil is linearized so that the effect from the thickness, camber, angle of attack and flap angle can be calculated separately, and the solutions can be added together to find the final result. There are some requirements that must be fulfilled for linear foil theory to be valid. The thickness must be much smaller than the chord length, angle of attack should be less than 10° and the camber to chord ratio must be small[37]. This means that linear foil theory cannot be used when flow seperation is present. Nevertheless, for fully turbulent flow Faltinsen esimated that linear foil theory is valid to approximately 13° to 17° angle of attack[13].

To analyse or simulate a flow around an object it is possible to use potential theory or one can solve the Navier-Stokes equation using CFD[13]. Potential flow theory is based around a velocity potential which is defined as in equation 4, here $\vec{u}$ is a velocity vector field. The use of the velocity potential gives a rotation free flow which is an acceptable approximation for a flow with high Reynolds number and is also good for analysing flow around a hydrofoil as long as the boundary layer is not considered[26]. Even though the boundary layer cannot be included in the potential flow calculations, the pressure distribution found using potential flow can

be used in a boundary calculation to for example find the location of separation or the displacement thickness[13].

$$\vec{u} = \nabla\phi \tag{4}$$

The lift force can be related to circulation. Circulation is a useful notation that can be related to vorticity through Stokes theorem, and is an important factor in propeller and foil calculations. It is a line integral with an arbitrary closed curve C over a velocity vector field, its definition is shown in equation 5[13]. Using potential flow on a foil with a sharp leading edge will give infinite velocity at the trailing edge. The Kutta condition states that the flow shall leave the trailing edge tangentially, so by introducing circulation this condition can be fulfilled. Another parameter of interest related to circulation is the induced velocity caused by the vortex core. Assuming a circular path, the definition for induced velocity r distance from the vortex core is seen in equation 6.

$$\Gamma = \oint_C \vec{U}\,d\vec{s} \tag{5}$$

$$U_{induced} = \frac{\Gamma}{2\pi r} \tag{6}$$

Kutta-Joukowski's theorem is given in equation 7 and shows the relation between the inflow velocity, circulation and lift. It is a combination of the induced velocity and the Bernoulli equation. In order to apply this to a foil the circulation can be distributed over the mean line and the double integral can be calculated to find the lift. Both conditions are important in the theoretical explanation of how lift is generated over a foil, and the Kutta condition is often used in numerical calculations to decide the magnitude of Γ[37].

$$L = \rho U \Gamma = \rho U \iint_C \gamma(x, y)\,dx\,dy \tag{7}$$

In this thesis only 2D flow is considered. This is an acceptable assumption as it will lead to conservative results with regards to the flap moment. When studying a 3D hydrofoil, the lift distribution in the span wise direction must also be considered. The circulation will not be constant along the span, but gradually become zero towards the edges. In order to fulfil Kelvin's theorem saying that *"For an ideal fluid acted upon by conservative forces (e.g. gravity) the circulation is constant about any closed material contour moving with the fluid"* [25] the concept of free

vortices or tip vortices is introduced, a simplified vortex system can be seen in figure 4. Also, a starting vortex will occur behind the foil. The starting vortex is assumed to not affect the flow around the foil in steady foil analysis as it is so far downstream. This results in the flow being analysed as a horseshoe vortex, and the free vortices will give an induced velocity called downwash. The downwash affects the inflow direction and results in a change in the lift and drag due to the change in the dynamic pressure[37].
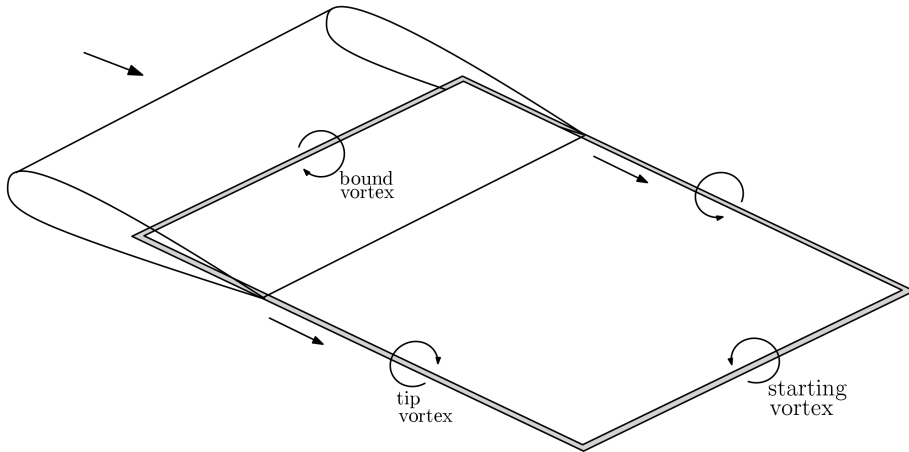
Figure 4: Vortex system around a 3D foil

3.1.1   Pressure distribution around a foil

A foil can be designed to give a desired pressure distribution, even though it can be difficult to obtain. As mentioned there will be a low pressure on the upper side of the foil, and a high pressure under the foil but there will also be local differences along the geometry. As seen in figure 5 there is a pressure peak at the leading edge which increases with increasing angle of attack. This pressure peak is caused by the sudden decrease in the fluid velocity when the leading edge disturbs the flow. At the leading edge there will be a stagnation point where the velocity is zero and the kinetic energy becomes pressure energy, this stagnation pressure is also called pitot pressure. A common way of describing pressure changes in a pipe or around an object is by the pressure coefficient C_P. This coefficient describes the relative pressure between the static pressure difference in the numerator, and the dynamic pressure difference in the denominator, as seen from equation 8[11]. The pressure coefficient close to a body is independent of the body size and is therefore very useful when evaluating flow around a foil.

$$C_p = \frac{p - p_\infty}{\frac{1}{2}\rho U^2} = \frac{p - p_\infty}{p_0 - p_\infty} \tag{8}$$
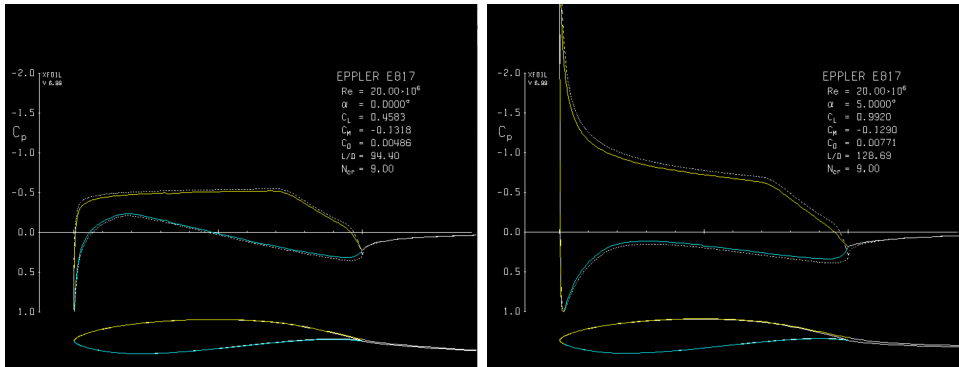
(a) EPPLER E817 with $\alpha=0°$ (b) EPPLER E817 with $\alpha=5°$

Figure 5: C_p distribution for EPPLER E817 at different angles of attack calculated in Xfoil with Re=$20 \cdot 10^6$. Solid line indicates viscous flow and dashed line indicates inviscid flow.
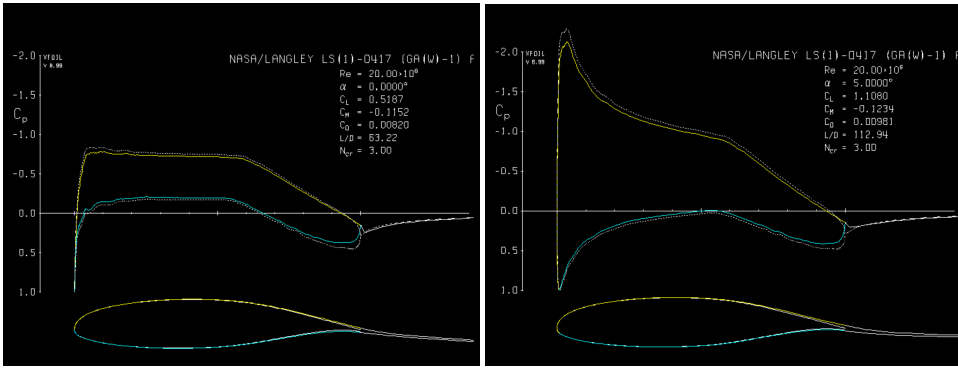
(a) NASA/LANGLEY LS(1)-0417with α=0° (b) NASA/LANGLEY LS(1)-0417 with α=5°

Figure 6: C_p distribution for NASA/LANGLEY LS(1)-0417 at different angles of attack calculated in Xfoil with Re=20·10⁶. Solid line indicates viscous flow and dashed line indicates inviscid flow.
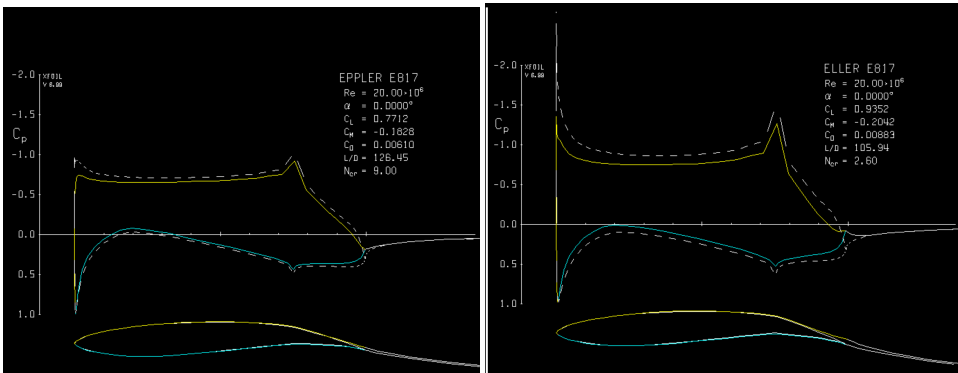
(a) EPPLER E817 with α=0° and α_f=5°   (b) EPPLER E817 with α=0° and α_f=9°

Figure 7: C_p distribution for EPPLER E817 with different flap angles calculated in Xfoil with Re=20·10⁶. Solid line indicates viscous flow and dashed line indicates inviscid flow.

In figure 5a and 6a the pressure distribution for EPPLER E817 and NASA/LANGLEY LS(1)-0417 as found in Xfoil can be seen. This demonstrates how the pressure differs from profile to profile depending on the shape. Changing the angle of attack

also affects the local pressure distribution as seen in figure 5b and 6b. Another way of affecting the pressure is by adding a flap to the foil profile. Having a flap with an angle at the trailing edge will influence the whole pressure distribution and can effectively be used to control the lift. In figure 7 it can be seen how the pressure distribution is affected by adding a flap with length of 0.25c with 5° and 10° angle. In addition to increasing the pressure peak at the leading edge there will be a new pressure peak close to the flap hinge.

3.1.2   Lift on foil with flap

The use of a trailing edge flaps on hydrofoils can enhance the lifting capability of the foil, a more even pressure distribution is obtained by increasing the effective camber rather than increasing the angle of attack. This can be seen if figure 5b and 7b are compared, the lift is approximately the same but the pressure peaks in figure 7b are smaller. When considering the risk of cavitation this is advantageous, as higher lift can be gained without the occurrence of pressure peaks. Faltinsen [13] derived an expression for both lift and hydrodynamic moment on a foil with flap. The equation for the moment applies to the centre of the foil and is not of particular interest in this study. The lift on the other hand can be compared to the results retrieved from the software applied in this thesis. Equation 9 is the expression for the lift, in order to compare it with the results from Xfoil and STAR-CCM+ it is made dimensionless as in equation 10.

$$L = 4\rho U^2 \mathrm{cr}^{1/2}\alpha_f \tag{9}$$

$$C_L = \frac{L}{0.5\rho U^2 c} \tag{10}$$

Here r is the flap length in percentage of the chord length and α_f is the flap angle. There are some assumptions and simplifications in this expression, such as the foil being symmetric and with zero camber [13]. This limits the appropriate use of the expression and it cannot be expected to give accurate results when cambe i.e. asymmetric geometry is analysed.

3.1.3   Unsteady thin-air foil theory

Foils do not always work under the steady conditions assumed in the previous sections. Heave and pitching motions or motions caused by waves affect the operation of a foil. Also, any sudden changes in lift will result in a different behaviour than the ones found under constant conditions. Analytic modelling of unsteady

behaviour is very useful to apply in understand the effects caused by the unsteady condition. Many such approaches are based on steady 2D thin foil theory, and Wagner, Theodorsen, Küssner and von Kármán & Sears have formulated results for unsteady air foil problems, both in the time and frequency domain[22]. The different solutions give different insight in the dynamic behaviour. Theodorsen's theory is a widely used solution for a harmonically oscillating 2D airfoil in inviscid, incompressible flow with only small disturbances. Wagner and Küssner are useful for estimating how much time it takes before the steady lift is reached when there are sudden changes in the inflow.

If the bound circulation on the foil changes, a vortex of equal magnitude and opposite direction must be created in the fluid in order to keep in line with Kelvin's theorem. This results in starting vortices that cause induced velocities which affect the circulation at the foil and the forces on the foil will change[22]. This was the behaviour Theodorsen described analytically for a harmonically oscillating foil. A sudden change in angle of attack will result in changed inflow and the lift will either increase or decrease. The lift will not change instantly, and this lift history is given analytically by the Wagner function, a curve-fit approximation of the function is shown in equation 11[37]. Here U is the velocity in front of the foil and t is time. Solving this equation for different chord lengths of travel shows that the lift has stabilised after about ten chord lengths of travel[37].

$$\frac{C_L(U\frac{t}{c})}{C_{Lt=\infty}} = 0.5 + 0.5 \cdot \sqrt{1 - (\frac{155 - U\frac{t}{c}}{155})(27.59)} \tag{11}$$

3.2   Panel method

One way of using the velocity potential to analyse flow is through the panel method. Here the analytic solutions for flow singularities such as sources, doublets and vorticity are used in a numerical scheme to solve the Prandtl-Glauert equation[12]. The Prandtl-Glauert equation is a simplified version of the Navier-Stokes equation, where the flow is assumed to be irrotational, hence velocity potential can be applied. In addition, all viscous, heat-transfer and nonlinear terms are neglected[12]. Disregarding the viscous effects means that separation and skin-friction drag will not be included, but as mentioned previously a separate calculation based on the pressure distribution from the potential flow can be used to account for some of the effects of the boundary layer.

The panel method has been very popular in analysing flow around aircrafts as

it allows for complex geometries in the calculations, and usually solve for both sub-sonic and supersonic flow. The geometry is broken down into panels and a source and doublet distribution is commonly used, then expressions for the influence-coefficients for the potential can be found. The matrix system is solved numerically, and the singularity parameters are found. The velocity can then be found at any point and this can be used to find the pressure distribution. The boundary conditions set for the system makes the solution fit the geometry [12]. It is important that the solution is unique or else the code will crash, in the early stages of designing panel method code this was a problem that frequently occurred. Since then many successful panel method codes have been developed such as PAN AIR, VSAERO and the Woodward-Carmichael code.

3.3   Boundary layer theory

The theory in this section is mainly based on H. Schlichting and K. Gerstens book *Boundary Layer Theory* [29], if not stated otherwise the equations and derivations can be found in this book.

In theory it is shown that Re$\to \infty$ is a good approximation to describe flows in many cases, as viscous effects do not greatly influence the flow above a certain velocity [29]. When this approximation is used, the no-slip condition at a body surface is neglected, and it is therefore necessary to include a transition layer between the open flow and the body surface. This transition layer has been named boundary layer and was first described by Prandtl in 1904 [10]. He divided the flow into a viscous inner layer and an outer layer that is assumed to be inviscid. The thin layer close to the wall can either be turbulent or laminar, along a flat plate it is typically laminar close to the leading edge and further down the plate there will be a transition to turbulent flow. The symbol $\delta(x)$ is often used to describe the boundary layer thickness, and looking at experimental data it can be seen that it is monotonically increasing with increasing x. When analysing boundary layer flow in 2D it can be assumed that δ is much smaller than the distance x, assuming x is in the inflow direction and y is normal to the body surface, hence it is possible to use the approximations shown in equation 12 [39].

$$\vec{v} << \vec{u} \qquad \frac{\partial}{\partial x} << \frac{\partial}{\partial y} \tag{12}$$

The simplest example is a laminar boundary layer on a flat plate with the flow parallel to the plate. This example is described in many books including Boundary-

Layer Theory by H. Schlichting and K. Gersten [29]. Figure 8 shows how a laminar boundary layer develops along a flat plate. It is important to remember that $\delta(x)$ is only a tool which can help to describe boundary layer flow and due to this there is no exact definition of the boundary layer thickness as the transition to the outer flow happens gradually. It is therefore common to define it with respect to the velocity in the outer flow, the edge of the boundary layer can be said to be where the velocity of the flow close to the wall is 99% of the free stream velocity, $0.99U_\infty$ [39]. Other interesting parameters in the boundary layer is the displacement thickness and friction forces. Here, displacement thickness is how much the streamline is shifted out of position by the boundary layer. It can be shown that the boundary layer thickness is proportional to $\sqrt{\frac{\nu x}{U_\infty}}$, and H. Blasius found the exact solution to the approximation to be $\delta_{99} = \frac{5x}{\sqrt{Re_x}}$.
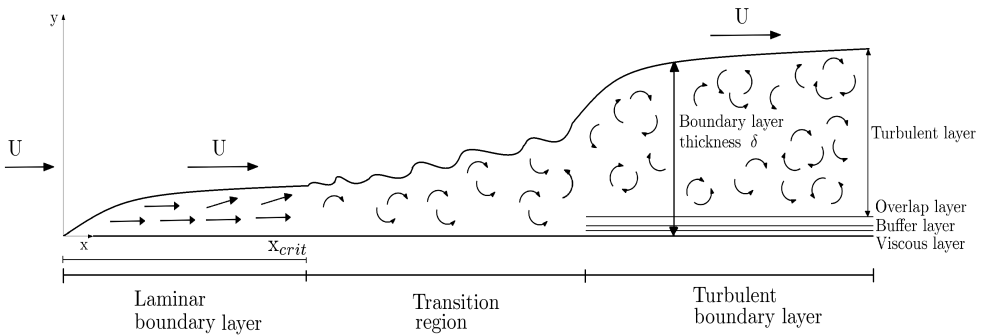
Figure 8: Development of boundary layer along a flat plate

When considering other shapes such as air foils the pressure differences due to the geometric shape has to be considered. The boundary layer will be laminar at the leading edge and then transition over to turbulent flow moving towards the trailing edge. The outer inviscid layer contributes with a pressure due to the shape of the air foil. This pressure will only be a function of x as the boundary layer is very thin compared to the curvature of the body and perpendicular pressure gradients can be neglected.

3.3.1   Turbulent boundary layer

The situation becomes somewhat more difficult to describe when turbulent flow is introduced. When the velocity of the fluid and the length of the plate increases

the laminar flow will become turbulent. At a given distance away from the leading edge, often called x_{crit}, the flow will become turbulent. This does not happen suddenly but over a distance where the flow is in transition between laminar and turbulent as seen in figure 8. Experimental measurements have resulted in an approximation of the turbulent boundary layer thickness of $\delta(x) = 0.14 \frac{\nu Re_x}{U_\infty ln(Re_x)} G$. Here G is a function varying with $ln(Re_x)$ but the variation is small, and G can often be set to a constant. In the region $10^5 < Re_x < 10^6$, G is approximately 1.5. The turbulent boundary layer will be thicker than the laminar and have two layers instead of one. The flow next to the body surface forms a very thin layer where viscous effects are dominant, this layer is called the viscous sublayer or inner layer. Outside theviscous sublayer there is a thicker layer where the fluctuating motions are dominant, here viscosity does not contribute to the fluid motion. Between these there is a transition which is called the overlap layer where both viscous and turbulent shear is important[13].

The turbulent flow is caused by the random fluctuating motion of small fluid volumes, these motions are very complex and difficult to describe mathematically. Prandtl showed that by the use of boundary layer the Navier-Stokes equation could be made simpler and used to calculate flow close to a body [10], unfortunately this leads to more unknowns than available equations in turbulent flow. It is therefore necessary to find a way to work around it, and this has been solved by using turbulence modelling. In turbulence modelling the remaining equations are obtained by modelling the relations between the mean fluid motion and the fluctuation, often by the help of empirical values[13], further described in section 3.5

3.3.2   Law of the wall

It is convenient to describe the velocity profiles close to the wall dimensionless to be able to describe each layer in non-separating flow with different velocity profiles with one mathematical relation. This can be achieved through the dimensionless distance from the wall y^+ (equation 13). Here u_τ is the shear velocity or friction velocity and τ_w is the wall shear stress.

$$y^+ = \frac{y u_\tau}{\nu} \qquad u_\tau = \sqrt{\frac{\tau_w}{\rho}} \qquad (13)$$

As the fluid behaviour in the inner and outer region of the boundary layer differ, different expressions for the different regions are needed to describe the flow. The law for the outer layer is also called the velocity-defect law, as it describes how

the outer fluid is slowed down by the wall effects. The flow behaviour in the inner layer can again be divided into three regions: the viscous sublayer, buffer layer and overlap layer. In the viscous sublayer where viscous shear is dominating, it can be shown that relation between u^+ and y^+ is linear such that $u^+ = y^+$, this is valid for $y^+ \leq 5$[39]. The overlap layer follows a logarithmic distribution and is therefore also known as the log-law region, it follows the relation in equation 14 where B is a constant and κ is the Karman constant. Here experimental results show good agreement for $30 \leq y^+ \leq 300$, which also includes some of the outer layer, the relation is usually only applied until the end of the inner layer at approximately $y^+ = 100$[39].

$$u^+ = \frac{1}{\kappa} ln(y^+) + B \tag{14}$$

In the buffer layer where $5 \leq y^+ \leq 30$ the velocity profile does not follow a specific distribution but is a smooth merge between linear and logarithmic functions. Until Spalding derived the expression seen in equation 15, each relation had to be applied separately for the appropriate layer. Spaldings expression is a good fit for the whole of the inner layer and is in good agreement with the results from an experiment conducted by Lindgren[39]. The different distributions can be seen in figure 9, with $B = 5$ and $\kappa = 0.41$.

$$y^+ = u^+ + e^{-\kappa B}[e^{\kappa u^+} - 1 - \kappa u^+ - \frac{(\kappa u^+)^2}{2} - \frac{(\kappa u^+)^3}{6}] \tag{15}$$

In CFD calculations it is convenient to apply logarithmic wall functions as this allows for a coarser grid at the wall surface, this can reduce computational time. For this to be valid it must be assumed that the turbulent flow is fully developed. To ensure that turbulent shear stresses dominate as viscous shear stress is not included in the logarithmic wall functions. This has proven to be a good approximation in many wall-bounded turbulent boundary layers and is commonly used in CFD calculations[11]. An estimate of the thickness of the first element can easily be found according to equation 16.

$$y = \frac{y^+ \mu}{\rho u_\tau} \tag{16}$$
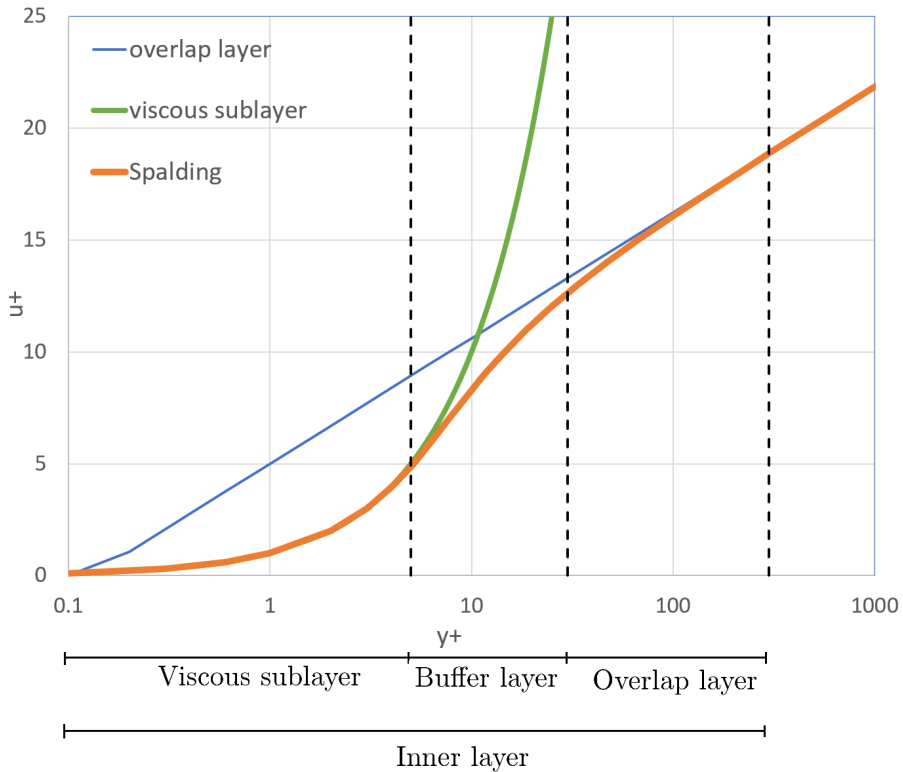
Figure 9: Law of the wall, with $\kappa = 0.41$ and B=5

3.4   Computational Fluid Dynamics (CFD)

Computational fluid dynamics is in one way fluids answer to Finite Element Method (FEM) used in structural analyses. Here the governing equations of Navier-Stokes and Laplace that will be shown in section 3.5 are solved in combination with boundary conditions. To the authors knowledge, this equation system has not yet been solved analytically, making it necessary to solve them using numerical schemes. The Finite Volume Method (FVM) is often applied to solve the governing equations by integrating them over the volume elements one by one. This is done by setting up a fluid domain which is partitioned into smaller volumes also known as meshing. The mesh divides the domain into smaller volumes, or in the case of a 2D solution, areas. Here, the refinement of the mesh is determined by each individual flow situation, and the change in the flow over one cell element must not be too large as this can lead to loss of information. Typically, it is necessary to

have a fine grid in the boundary layer or at other locations with large velocity gradients or pressure variations. In areas of the fluid domain where there are smaller variations, larger cell sizes will give satisfactory results. To enable modelling of turbulence without trying to solve the small-scale perturbation caused by turbulence, turbulence models and wall treatments are applied. The turbulence models help to close the so-called closure problem related to the solution of the governing equation system, this will be discussed in the following sections.

3.5   RANS equation and turbulence modelling

The motion of viscous fluids can be described by the Navier-Stokes equation seen in equation 17[11]. When analysing turbulent flow it is possible to solve the N-S equation directly through Direct Numerical Simulation (DNS). Unfortunately this requires an extremely fine grid in 3D and the computational power and time required would be immense[11]. Another way of solving this is through Reynolds-averaged Navier-Stokes equation or RANS equation. Here the parameters of interest are decomposed into mean flow and fluctuation, this is done for all the velocity components as well as pressure, time and density i.e. $u = \bar{u} + u'$. $\bar{u}$ is the average over the turbulence time scale and u' is varying with the turbulence time scale[13]. The fluctuation part influences the mean velocity, resulting in an apparent added resistance in the fluid. This effect has been called apparent viscosity and is central for all theoretical turbulence modelling. This leads to an additional term with shear stresses known as apparent stresses or Reynolds stresses which are accounted for here[29]. The continuity equation seen in equation 18[11] is applied to set up the RANS equation.

$$\rho \frac{D\vec{U}}{Dt} = -\vec{\nabla} P + \rho \vec{g} + \mu \nabla^2 \vec{U} \tag{17}$$

$$\frac{\partial \rho}{\partial t} + \vec{\nabla} \cdot (\rho \vec{u}) = 0 \tag{18}$$

The decomposed parameters can be inserted into equation 17 and 18 and by definition the time average of the fluctuation will be zero (i.e. $\bar{u}' = 0$). This results is the momentum equation for incompressible flows in equation 19[27], here tensor notation is used. The $\overline{\rho u_i' u_j'}$ term is the apparent turbulent stress tensor also called turbulent shear, and $\overline{\tau_{ij}}$ represents the laminar viscous stresses.

$$\frac{\partial}{\partial t}(\rho \bar{u}_i) + \frac{\partial}{\partial x_j}(\rho \bar{u}_i \bar{u}_j) = -\frac{\partial \bar{p}}{\partial x_i} + \frac{\partial}{\partial x_j}(\overline{\tau_{ij}} - \overline{\rho u_i' u_j'}) \tag{19}$$

Where

$$\overline{\tau_{ij}} = \mu(\frac{\partial \bar{u}_i}{\partial x_j} + \frac{\partial \bar{u}_j}{\partial x_i}) \tag{20}$$

The Reynolds stresses contribute with more unknowns, and more equations are necessary in order to solve the system.

The equation for the kinetic energy of turbulent fluctuation also known as the k-equation defined in equation 21(using Einstein summation notation) is often added to account for turbulence conservation[39]. The equation describes the energy balance in turbulent fluctuation and helps in understanding the physical aspect of the turbulent boundary layer. It can be derived into the turbulence kinetic energy relation which can be divided into convection, turbulent diffusion, viscous diffusion, turbulent production and dissipation[29].

$$k = \frac{1}{2}\overline{u'_i u'_i} \tag{21}$$

As mentioned above the issue in solving the turbulent flow problem lies in the lack of available equations for the unknown parameters, this is known as the closure problem. The k-equation is part of solving this, but other balances are also needed to close the problem. Several such solutions have been suggested in the form of turbulence models and they are commonly divided into zero-equation models, one-equations models, two-equation models and so on depending on how many partial differential equations are necessary to close the problem. Zero-equation models are also known as algebraic turbulence models where the two most common are the eddy viscosity model and mixing length model.

The most relevant models for this thesis are the two-equation models such as the k-ε model and the k-ω model. Two-equation models use two extra transport equations to account for turbulence effects like diffusion and convection of energy[8]. As the names indicate, both use the k-equation as part of the solution, here the k-equation says something about the turbulence energy and the other determines the scale of the turbulence. The Boussinesq eddy-viscosity assumption is the basis of the two-equation models and is the biggest strength and weakness of the models[8]. The assumption states that the Reynolds stresses are proportional to the strain-rate tensor. The strength is that it simplifies the calculations, in addition to allowing the introduction of more intuitive turbulence parameters. On the other hand, this assumption is not valid if the flow is greatly accelerated or

decelerated or is exposed to large curvatures. This results in the assumption not being generally valid.

The k-ε model uses the turbulence kinetic energy k-equation and turbulence dissipation rate ε to close the problem. The dissipation rate is the rate that the kinetic energy is transformed to thermal internal energy[8]. This model has its limitations but has been shown good for free shear layer flows with small pressure gradients [3]. The k-ω model applies the specific turbulence dissipation rate ω and is better at modelling near-wall interactions[4] as well as having good numerical stability and no damping functions are necessary[23]. Unfortunately, it is very sensitive to the ω values in the free-stream and is not good for wake calculations[23]. Improvements to already existing models are suggested regularly and one of the most applied is Menters SST k-ω model which exploit the strengths of the different models, described in the following section.

3.5.1   SST k-ω turbulence model

SST is short for shear stress transport, and in his suggestion Menter combines the k-ω and k-ε with a shear stress transport model, which resulted in great improvement of both existing models[23]. The SST k-ω model has become very popular and results show that the model gives good values for flows with adverse pressure gradients and separation[7]. Menter's SST model combines the k-ω and k-ε models with blending functions determining where the different models should be used in the flow problem. The transport equations for k and ω according to Menter's SST model can be seen in equations 22 and 23[24].

$$\frac{\partial(\rho k)}{\partial t} + \frac{\partial(\rho U_i k)}{\partial x_i} = \tilde{P}_k - \beta^* \rho k \omega + \frac{\partial}{\partial x_i}[(\mu + \sigma_k \mu_t)\frac{\partial k}{\partial x_i}] \tag{22}$$

$$\frac{\partial(\rho \omega)}{\partial t} + \frac{\partial(\rho U_i \omega)}{\partial x_i} = \alpha \rho S^2 + \beta \rho \omega^2 + \frac{\partial}{\partial x_i}[(\mu + \sigma_\omega \mu_t)\frac{\partial \omega}{\partial x_i}] + 2(1 - F_1)\rho \sigma_{w2}\frac{1}{\omega}\frac{\partial k}{\partial x_i}\frac{\partial \omega}{\partial x_i} \tag{23}$$

The blending function F_1 will be zero away from the body surface and activate the k-ε model, and equal to one in the boundary layer activating the k-ω model. $\beta, \beta^*, \sigma_k, \sigma_\omega$ and σ_{w2} are constants determined by the model they represent[24].

3.6   Courant-Friedrichs-Lewy condition

In numerical calculations it is important to ensure numerical stability, if this is not maintained the solution might converge towards an incorrect answer or not

converge at all. Numerical solutions can either be explicit or implicit and the stability of these are very different. An explicit solution only uses the values found at the current step to find the values at the next step, the calculations will therefore easily become unstable if precaution is not taken. An implicit solution scheme uses the known parameters at the current step and the unknown parameter in the next step to find the correct values in the next step. This makes the computational demands much higher as more calculations are necessary for each numerical step, but the solution is more stable. For an unsteady solution the time-step is a critical stability factor and the stability criterion that should be satisfied is the Courant-Friedrichs-Lewy condition also known as the CFL-condition shown in equation 24 for one dimension. Here Δt is the time step, Δx is the element size and u is the fluid velocity. For an explicit solution the Courant-number should be around one as too much information is lost if the timestep is too large and the solution will become unstable. On the other hand, if too much unnecessary information is included it may degrade the solution, so the CFL should not be much less than unity either[27]. For an implicit solution this number is not so crucial in regards to stability, but if too large timesteps are used the solution might converge towards an inaccurate solution[1]. The computational time and power available and how accurate a result is desired determines the acceptable value of the Courant-number. Typically, a time-independency study should be conducted when analysing unsteady flow to find an appropriate Courant-number.

$$CFL = u\frac{\Delta t}{\Delta x} \tag{24}$$

3.7 Sources of error in numerical computation

If numerical calculations are used to solve an analytic problem, there will always be some sort of deviation from the exact analytical solution. This is something that must be kept in mind when applying numerical solutions in computational problems, numerical errors must be expected. There are three main sources of errors in numerical computation: round-off error, data uncertainty and truncation errors (or discretization errors) [17]. It is often easier to identify the errors caused by data uncertainty than errors caused by rounding. Errors caused by data uncertainty can originate from errors in the storage of the data, bad measurements or estimations.

Some fractions will have an "infinite" number of digits, unfortunately there is a limitation to how many digits of a number a computer can store. The software will round of the value to a given number of digits which it can use for further

calculations. This rounding may occur in each iteration step and accumulate with time and the results from the analysis might become invalid. On the other hand, rounding errors have also been known to cancel each other in stable algorithms, making the final result more accurate than the individual calculations. Rounding may also lead to instabilities in the calculations, these are often caused by a few rounding errors with insidious growth[17].

Truncation or discretisation error is unavoidable in any numerical calculation, this is the error that occurs when an infinite sum is made finite. It can be seen in Euler's and Newton's method which are derived from the Taylor series, here the infinite sum is made finite and the error related to the *step size h* can be approximated. In CFD the step size is related to the mesh, so it emphasizes the urge to conduct a mesh (or grid) independency study in analyses based on numerical calculations.

4 Computational fluid dynamics in STAR-CCM+

STAR-CC+ is a commercial software produced by CD-Adapco and recently bought by Simens. STAR-CCM+ is a user-friendly program with an intuitive interface which includes a tutorial library that guides users through many examples. On the downside the code is proprietary which can make it difficult to explain unexpected results. They may be due to wrong input values, wrong use of solvers or some bug in the program. Also, the program will run an analysis almost regardless of input values, making it easy for an unexperienced user to accept wrong results as a proper solution to the problem at hand. CFD programs are very complicated, so the average user would not be able to understand the code even if it was open source. So, using a proprietary program should not be a problem if it is used with caution and within its limits. When applying STAR-CCM+ one must rely on the tutorials and the recommendations given by the producer of the software when solving a problem.

STAR-CCM+ solves the Navier-Stokes equation using finite volume method, which means it discretises the volume into smaller cells and approximates the integrals over each cell. The surface and volume integrals are approximated using points at the face of the cell and in the middle of the cell respectively. Several methods for solving the issue with turbulence and the velocity-pressure coupling is offered in this software. STAR-CCM+ is a very comprehensive state-of-the-art software which allows for a broad spectrum of analyses, hence there are a lot of choices to be made when setting up an analysis. Further elaboration of the solvers and physical models used in this report will follow in the next sections.

4.1 Foil geometry

The foil geometries tested are the *EPPLER E817* and *NASA/LANGLEY LS(1)-0417*, and the geometry coordinates are retrieved from airfoiltools.com. The geometries were chosen as they are both standard foils with camber. They have good operational properties and the *EPPLER E817* is designed to perform well as a hydrofoil[2][5]. In order to get the geometry represented in STAR-CCM+ the CAD software *Autodesk Inventor Professional 2017* was applied. The coordinates for the geometry were used to draw a solid model with a flap before the geometry was exported as an *.stp* file. A small gap was inserted between the wing and the flap and the bottom edge of the wing was rounded, this was to ensure that STAR-CCM+ interpreted the parts as two separate bodies and that the flap and wing did not interact when a flap angle was introduced. This gap might influence the calculations, but it is considered to be negligible for the results retrieved in this

thesis. If the flow was to be studied in detail it would be necessary to look further into the influence of this gap.

Different flap sizes were also studied for both foil geometries. Each wing was made with flap lengths of 0.1c, 0.25c and 0.4c (where c is the total chord length) to see how this affected the forces acting on the hydrofoil. In figure 10 the *EPPLER E817* geometry is shown with the different flap sizes.
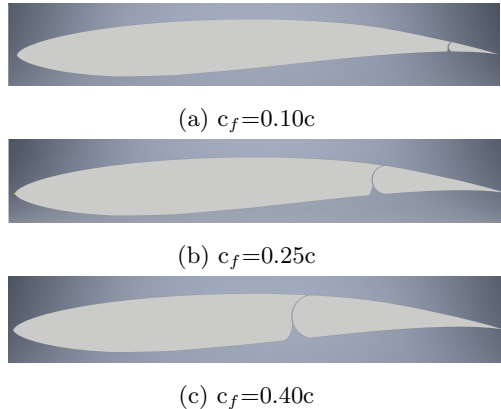
(a) c_f=0.10c

(b) c_f=0.25c

(c) c_f=0.40c

Figure 10: Lift on EPPLER 817 with different flap lengths, α_f=0°

The domain was then added in STAR-CCM+ to enable the possibility of changing the domain size directly in the software.

4.2 Grid design

In order to perform a reliable CFD study it is important to use an appropriate grid design. STAR-CCM+ provides an integrated mesh generation system and it allows the user to choose between a tetrahedral, polyhedral or trimmed mesher topology. In addition, it is possible to enable a prism layer on surfaces where wall effects are important. The trimmed and polyhedral topologies give the most accurate solutions, but the construction of the grid and calculations are more time-consuming for these than the tetrahedral mesh. Any of the meshers will give grid independency given that the element density is high enough[36]. STAR-CCM+ also allows for pure 2D meshing, this is much more time efficient and will give just as accurate solutions as a volume mesh with only one element thickness[35]. In this study 2D foil geometries are studied, hence a 2D mesher is applied. Unfortunately, it is not possible to choose trimmed mesher for the 2D mesher, so polyhedral mesh was

used. Polyhedral mesher uses arbitrary polyhedral cell shapes to create the core
mesh, where a dualization scheme is used with an underlying tetrahedral mesh
from which the polyhedral mesh is created[32].

The main parameters optimised in this study are listed below, all parameters can
be set as an absolute value or a relative value of the base size.

- *Base Size*: Characteristic value which other relative parameters can be based
  on
- *Target Surface Size*: The element size the surface mesh aims at in the absence
  of a mesh refinement
- *Minimum Surface Size*: The smallest element size allowed in the surface mesh
- *Surface Growth Rate*: The rate at which the element size grows from a refined
  mesh to the surface mesh
- *Number of Prism Layers*: Number of prism layers at the geometry surface
- *Prism Layer Stretching*: Determines the thickness of each prism layer
- *Prism Layer Total Thickness*: Total thickness of the prism layer

A default value must be set for all the parameters determining the 2D mesh, in
addition it is possible to customize the values of individual areas at the surface
and the edges in order to achieve refinement where it is needed. These values were
determined with an independency study and the results can be seen in section
5.1. In addition to determining the grid parameters the domain size must also be
checked. This was done through a separate independency study to make sure the
domain edges do not influence the flow around the foil.

4.2.1   Prism layer mesher

The variables will have rapid changes in the boundary layer, i.e. the velocity gra-
dient will be large. The best way of solving finit-difference schemes with fluid flows
is with a computational domain with equally spaced rectangles[38]. So, in order
to resolve the flow near the body surface accurately it is necessary to have a fine
systematic mesh in thisarea, and the prism layer mesh tool allows for this. The
prismatic cells resolve the boundary layer and allows for a more accurate adapta-
tion of the wall function as the thickness of the prism layer directly influences the
y^+ value. The thickness and number of prism layers recommended depends on the
flow situation. If the viscous sublayer is to be resolved more prism layers in the
cross-flow direction are necessary than for a shear turbulent layer. If wall functions
are used the y^+ value should be in the logarithmic layer, that is between 30 and
200-300 as seen in section 5.4. In addition to giving better control control over

the wall function the prism layer limits the numerical uncertainty by reducing the numerical diffusion close to the wall[33].

In the analysis presented in this report wall functions are applied so a coarser mesh can be used to limit the computational time. The velocity field along the foil geometry will vary substantially, hence the y^+ value will also differ along the body, it is therefore attempted to keep the average y^+ value close to 60. Even though STAR-CCM+ has an *All y+* wall treatment the y^+ will be kept between 30 and 100 as far as possible to avoid unnecessary uncertainties.

4.2.2   Overset mesh

Overset mesh or overlapping mesh can be used in STAR-CCM+ to simulate motion in analysis, it is also convenient to apply if multiple bodies are analysed simultaneously. The overset mesh can be set in motion during an analysis and can for example be used to simulate a rotating fan. The concept is to have a background mesh and then have a separate mesh surrounding just the body which is moving. The solution is based on sub-domains where only a sufficient overlap between the meshes is necessary to couple the solutions in the two grids. In such a mesh set-up one differs between three types of cells: *discretisation cells* also known as *active cells* where the governing equations are discretized, *interpolation cells* which obtain the solution from interpolation and *inactive cells* that do not participate in the solution.

The inactive cells are the cells that are covered by the bodies that are being analysed. Because the mesh is moving it is necessary to have cells behind the bodies, so they can be activated when the body moves. At the same time, it is important to keep these cells from affecting the overall result, so the cells which at any time are covered by a body are deactivated. This is solved by creating an artificial boundary in the background mesh. Next to such a boundary is the overlap layer where the variables in the cells obtain their solution from interpolation with the other grid. These host cells which are used to find the solution are also called donor cells, and how many donor cells are necessary for each interpolation cell depends on the interpolation scheme. To achieve a strong coupling between these grids the solution is considered in all cells in all grids simultaneously, this also gives a unique solution and the basic idea is that a linear equation system is solved for all grids at the same time.

It is possible to have several overset mesh on one background mesh. To solve

this there exists a mesh hierarchy to decide which cells are to be inactive, this lev-
elling of the grids is specified in the grid generation. It is not easy to incorporate
this in a code and it is difficult to define the hierarchy correctly. This can result in
the solution being calculated at more than one grid, if this occurs it is usually over
such a small area that the overall solution will not be affected. A more detailed
description of the overset mesh theory can be found in Hadzic's doctoral thesis
*Development and Application of a Finite Volume Method for the Computation of
Flows Around Moving Bodies on Unstructured , Overlapping Grids*[16].

In this thesis it was attempted to use overset mesh to see how the dynamic changes
of the flap angle affects the hydrodynamic forces, especially the hinge moment. It
would also have been interesting to see how the dynamic change of angle of attack
affected the force distribution with regards to the hinge moment. Unfortunately,
due to some difficulties regarding the simulations and the limited time available
no applicable results were obtained for these simulations. Several attempts were
made in completing the dynamic analysis, but the attempts failed every time. The
error messages given by the software were very scarce and finding the cause for the
solution failure was a challenge.

The first attempt at completing a dynamic analysis overset mesh was not ap-
plied at all. Here a sliding mesh using *Reference Frame* provided by STAR-CCM+
was used. A tutorial for a rotating fan found on the tutorial website was followed
and the same procedure was used for a foil with moving flap. Unfortunately the
simulation did not behave as expected, the fluid domain did not adapt to the flap
motion and an empty space was left where the flap initially was located as seen
in figure 11. After some time of troubleshooting and studying the user manual no
solution or explanation for this was retrieved, this behaviour might be due to the
way the foil is incorporated in the domain. The foil and flap were imported as
bodies and the domain was added in STAR-CCM+. The wing and flap were then
subtracted from the domain and the flap section and the domain were then set up
as two different regions with an interface. Another alternative would have been to
add the domain in the CAD software and create the mesh there as well, to mesh
the flap while it was a body and not an open space in the domain.

As the attempt of using motion to conduct the dynamic analysis failed, overset
mesh was applied. First an overset mesh was placed around the flap and the wing
was subtracted from the background mesh constituting the fluid domain. This
resulted in the wing disappearing in the simulation. It was then attempted to set

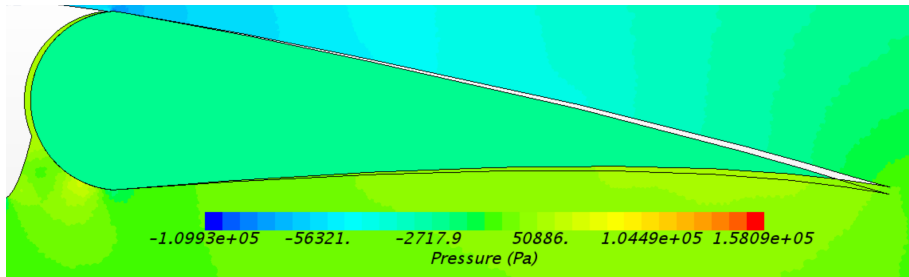two separate overset mesh over the wing and flap, in addition to the background mesh.

Figure 11: Attempt to conduct a dynamic analysis for moving flap using *Motion* in STAR-CCM+

This looked promising, but the software was not able to adapt the active and inactive cell correctly during the simulation. The cells occupying the last part of the wing became active even though they should have been inactive since they were covered by the wing. This resulted in extreme loads on the flap hinge and the results were not realistic.
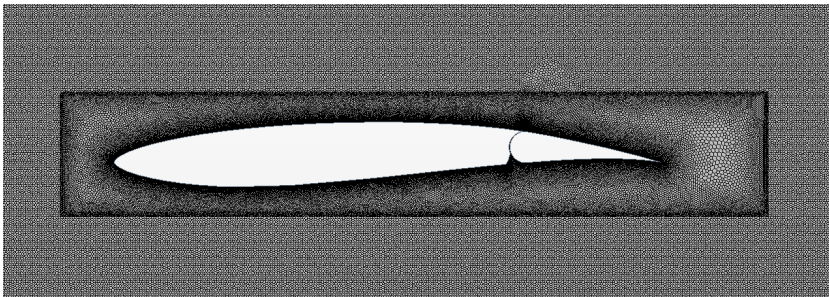
Figure 12: Mesh with overset mesh surrounding the hydrofoil

As a last attempt one overset mesh was applied to the whole foil to analyse the effect of dynamically changing angle of attack, as seen in figure 12. Once again, an issue with the mesh occurred, the error message stated that at some time-step there were not enough donor cells for the interpolation cells. This is usually due to too coarse or too fine mesh, or that the cell size in the two overlapping grids are too different. Some time was spent trying to refine the mesh, in the whole overset mesh and the overlap region, with no success. As adapting the mesh did not resolve the issue and due to lack of information in the error message the problem remained unsolved.

4.3   Boundary and initial conditions

Boundary conditions have to be set for the domain edges and the foil surface, the boundary conditions available in STAR-CCM+ and that are applied in this study are listed below.

- *Velocity inlet*: Is often used as inlet flow and utilises the know parameters of velocity and temperature (for compressible flow) to find the volume, momentum and energy flux
- *Pressure outlet*: The unknown parameters at this boundary are calculated from the interior of the domain using reconstruction gradients
- *Symmetry plane*: Here the shear stress will be zero
- *Wall*: Represents an impermeable wall and in viscous flow the no-slip condition is applied. No-slip condition implies that the fluid at the wall will have the same velocity as the wall, i.e. for a stationary wall the fluid velocity will be zero at the wall surface[11]
- *Overset Mesh*: This defines the overlapping boundaries between the overset mesh and background mesh, preparing it for interpolation. This boundary condition is set at the edges of the overset mesh

The initial condition for the analysis conducted in this thesis is the velocity inlet which is set to give the desired Reynolds number of $20 \cdot 10^6$, this corresponds to a foil speed of approximately 35 knots.

4.4   Physical models and solvers

Physical models are used to represent the physics in the numerical solution, and a combination of the physical models available in STAR-CCM+ are necessary in order to model the flow and find a solution. The physical models again decide which solvers are necessary to analyse the flow.

- *Steady*
- *Implicit Unsteady*
- *Two Dimensional*
- *Turbulent*s
- *SST (Menter) K-Omega*
- *K-Omega Turbulence*
- *Segregated Flow*
- *Reynolds-Averaged Navier-Stokes*
- *Liquid*

- *Gradients*
- *Exact Wall Distance*
- *Constant density*
- *All y+ Wall Treatment*
- *Partitioning*
- *Wall distance*
- *K-Omega Turbulent Viscosity*

These are the physical models and solvers applied in all the analysis in this report, where the implicit unsteady solver is used for large flap angles and the steady solution is used for small angles. This is done to limit the computational time as the unsteady solution is much more time-consuming than the steady. The reason for this being necessary is that at a given flap angle, separation might occur some distance from the trailing edge resulting in divergence of the steady solution, making it necessary to compute the unsteady flow. Segregated flow activates the segregated flow solver which calculates the momentum equation one dimension at the time using the *SIMPLE algorithm*, and the momentum and continuity equation connection is found through a predictor-corrector method[34]. These algorithms are commonly used in numerical analysis, but an elaboration of these is considered beyond the scope of this thesis, but an outline of the steps in the SIMPLE algorithm follows.

SIMPLE is short for Semi-Implicit Method for Pressure-Linked Equations and is a widely used algorithm for solving the Navier-Stokes equation. It can be summarised as follows: the boundary is set before the velocity and pressure gradients are computed. The discretised momentum equation is solved to find the intermediate velocity field, and the pressure correction equation is solved to find the cell values of the pressure correction. The pressure field is updated applying an under-relaxation factor, so the boundary pressure correction can be found. After that follows a correction of the face mass fluxes and cell velocities, and finally it starts all over again until it arrives at a solution. A more detailed elaboration of the algorithm can be found in the book *Computational Fluid Mechanics and Heat Transfer*[27].

4.5   Convergence criteria

Deciding when a solution has converged can be difficult as numerical disturbances may be present. STAR-CCM+ allows for different stopping criteria for each analysis, such as a maximum number of iterations, convergence of coefficients, or maximum physical time in unsteady analysis. In this report different convergence criteria were set for steady and unsteady simulations. For the steady simulation the solution was said to be converged when the lift coefficient had a relative change of $1 \cdot 10^{-4}$ over the last 80 iterations and a minimum of 1500 iteration steps had been completed. The number of minimum iterations was set after evaluating lift coefficient plots for some simulations. It was noticed that the solution seemed to converge after only 2-300 iterations steps before it diverged from this value and started to converge again around iteration step 1000. For the unsteady analysis the stopping criteria was set to a physical time of 3.0 seconds which corresponds to a foil movement of about 50c when Re$\approx 20 \cdot 10^{6}$, this was seen to give stable lift and drag coefficients.

In the unsteady analysis given number of iterations called inner iterations are performed within each timestep, the number of iterations determine how stable the calculation is. The more inner iterations are performed, the larger the time-step can be without the solution becoming unstable. For this case it is determined that a Courant number of 10 gives good results (see section 5.3), this corresponds to a time-step of 0.0005s and the number of inner iterations can be quite small. To ensure that the solution is maintained steady the number of inner iterations is set to 5. Still a time-step study should be conducted to find a suitable time-step in the unsteady analysis.

4.6   Moment evaluation

To find an appropriate actuator for controlling the flaps on a hydrofoil vessel it is necessary to expose the foil to different circumstances and conditions. In this report the hinge moment for different flap angles is found, it is also investigated how the angle of attack affects the moment. It would also have been interesting to see how dynamic effect affect the hinge moment as a stability and manoeuvring flaps will constantly operate under dynamic conditions.

Testing the foil with different flap angels is an important step to finding the maximum force the actuator will have to withstand in order to keep the flap in place. This is done by analysing the foil with different flap angles to find the most critical

value, and the simulations were run with a flap angle interval of 2°. This was completed for all the different flap chord lengths and both the foil geometries. The analysis were kept steady up to 8° and for the remaining analysis an implicit unsteady solution was applied. The force coefficients for lift, drag and moment were logged in .csv files and plotted in LaTex to compare the results.

Angle of attack will also affect the pressure distribution, and this might contribute to the hinge moment. To check the influence of the angle of attack the EPPLER E817 and NASA/LANGLEY LS(1)-0417 profile with flap length of 0.25c and 0.1c respectively were tested for 3 different angles of attack, 0°, 5° and 10°. The profiles with flap lengths of 0.25c and 0.1c were tested as these lengths appeared to be the most appropriate based on the flap angle tests, see section 7.

Unfortunately, no dynamic analysis were successfully conducted in this report due to lack of time to find the reason for the error messages appearing when using overset mesh. The idea was to change the flap angle with different velocities to observe how this affected the hinge moment. The hydrodynamic forces might be affected by the speed of the flow changes and it would have been interesting to investigate this further.

5   Independency study

To obtain reliable results in CFD it is important to design a set-up that does not influence the results. Here independency studies with respect to grid design, domain size and time-step are presented.

5.1   Grid and domain independency, EPPLER E817

The fist prism layer thickness is calculated according to equation 16 using the C_F given in the same section. This results in a first layer thickness of approximately $8.22 \cdot 10^{-5}$m assuming the chord length is one meter. This value is doubled and used as the basis for estimating the thickness of the first prism layer, as equation 16 gives the location of the centre of the cell, not the edge. The STAR-CCM+ online manual recommends in excess of 10-20 prism layers. After a brief evaluation of some early analyses 8 prism layers were found to be sufficient. Figure 13b shows how the lift coefficient changes with the base size. Figure 14b shows the change in percentage, by dividing the relevant lift coefficient by the lift coefficient found with the smallest base size. The lift varies a little with changing base size, but from figure 14b it can be seen that the value varies with only 1% and 2%, so a base size of 0.001 is considered sufficient to retrieve reliable results. A larger base size is not used as it is desired to stay comfortably within the convergence area. The results and parameters changed in the convergence test can be seen in table 2, here the base size was changed and the other parameters were set as a percentage of the base size. Some numerical disturbance is always to be expected, these will give some unevenness in the results regardless of the base size and may explain the small lift variation.
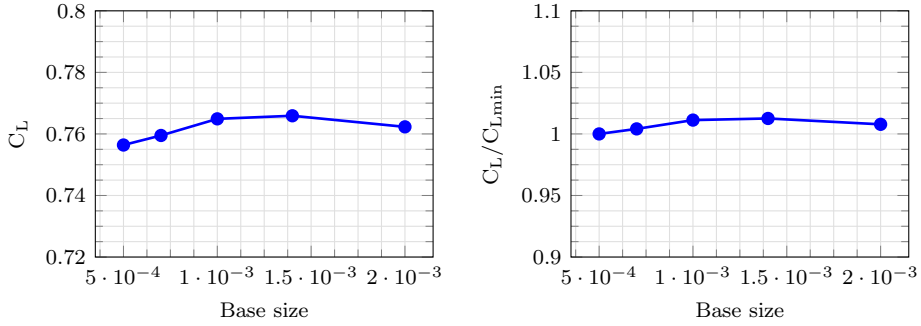
(a) Lift coefficient plotted against the smallest base size (element size) in the domain

(b) Lift coefficient for the base size divided by the lift coefficient for the smallest base size plotted against base size
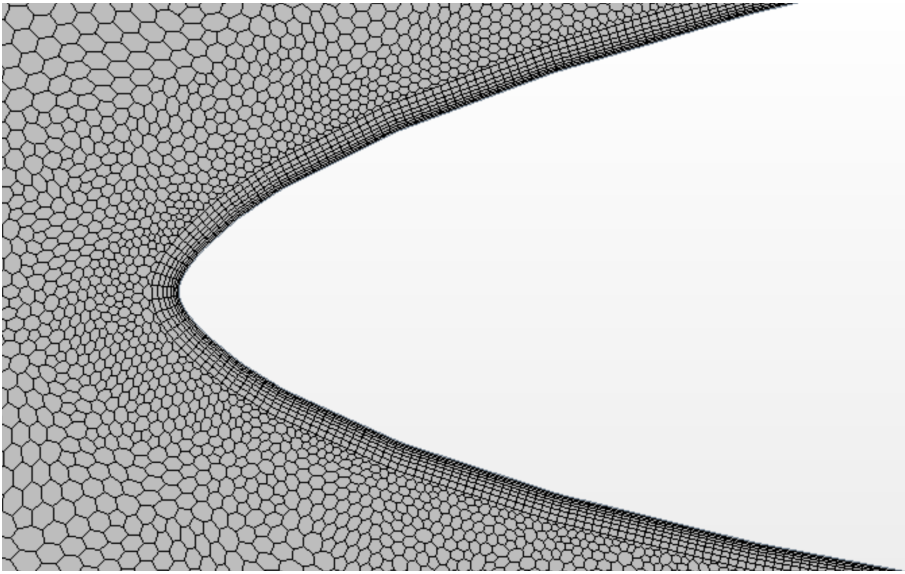
Figure 13: Mesh independency study for EPPLER E817 with c_f=0.25c and α_f=5°
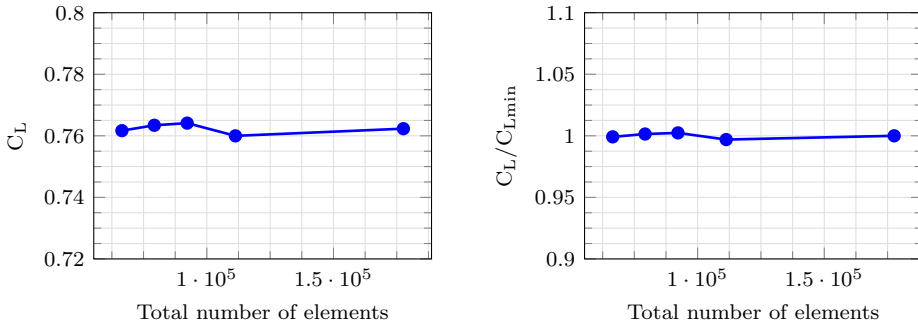
(a) Lift coefficient plotted against the total number of elements in the domain

(b) Lift coefficient for the base size divided by the lift coefficient for the smallest base size plotted against total number of elements in the domain

Figure 14: Domain independency study for EPPLER E817 with c_f=0.25c and α_f=5°

If the domain edges are too close to the foil they may affect the calculations and deteriorate the results, so a domain independency study is also conducted. Much the same is seen here as for the grid independency study and the variation in percentage is less than 1% for all the domain sizes. To make sure the domain does not affect the results the total number of elements is kept between 90 000 and 100 000 elements.

The final mesh design for the EPPLER E817 profile can be seen in figure 15, here the results from the *fine* mesh is used. The prism layer seen in figure 15a is approximately the same thickness around the whole foil and the element size right outside the prism layer is 1‰ of the chord length. For the five chord lengths behind the foil the base increases to about 10-15%, and for the remaining parts the element size varies between 15-25% of the chord length. In order to simplify the pre-processing, it was decided to use one continuous mesh in the whole domain, in addition, as it ensures consistency between the analyses as there are less parameters to keep track of. It would have been possible to have a finer mesh only in the wake of the foil so that the general element size could be larger.

Table 2: Mesh convergence study results with flap angle of 5°

|	Extremely fine	Very fine	Fine	Medium	Coarse
Base size	0.0005	0.0007	0.001	0.0014	0.002
Surface growth rate	1.06	1.06	1.06	1.06	1.06
Prism layer thickness	0.0016	0.00224	0.0032	0.00448	0.0064
Prism layer stretching	1.25	1.25	1.25	1.25	1.25
Number of prism layers	8	8	8	8	8
y^+	35.1	46.3	62.9	85.0	118.3
Number of elements	236149	142918	92236	61854	44082
C_L	0.7564	0.7595	0.7649	0.7659	0.7623
C_D	0.008499	0.008494	0.008461	0.008556	0.008704
C_M	0.01524	0.01537	0.01557	0.01565	0.01555

(a)
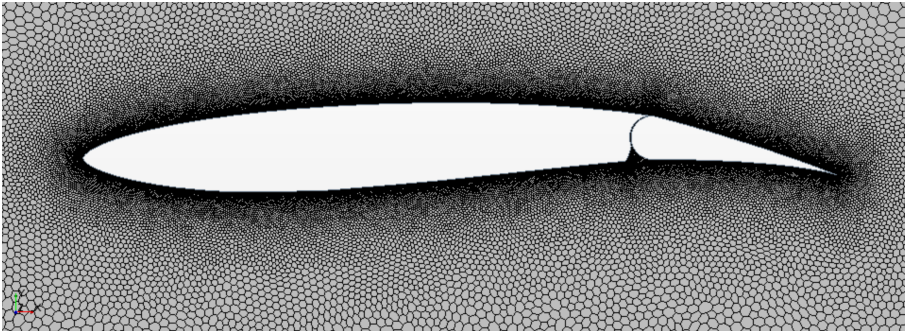
(b)
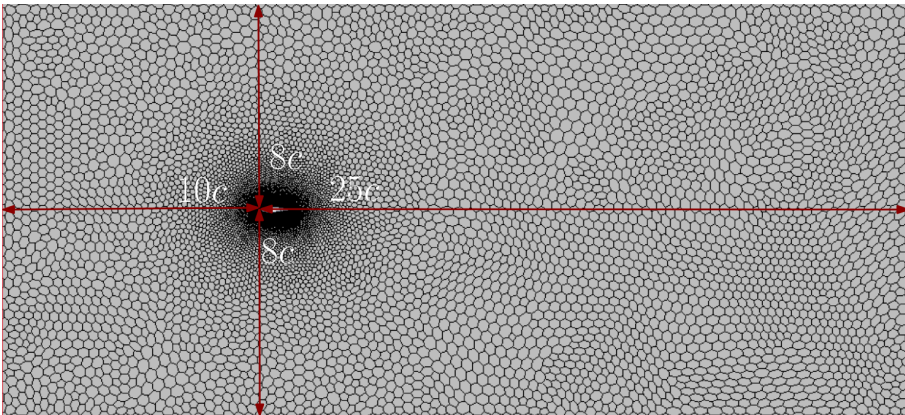
(c)

Figure 15: Mesh design for EPPLER E817

## 5.2   Grid and domain independency, NASA/LANGLEY LS(1)-0417

The geometric shape of this profile is quite different from the EPPLER E817 profile and a grid and domain independency study is conducted for the NASA profile as a precaution. The procedure is the same as for the EPPLER E817 geometry and the results can be seen in figure 16 and 17. The results show much the same tendencies as previously, and the percentual change in the lift coefficient is 1-2% which is acceptable. It was therefore decided to use a base size of 0.001 as for the EPPLER profile, and apply the same settings as for the fine mesh showed in table 2. The total number of elements was also between 90000-100000 so that the domain edges would not affect the flow around the foil.
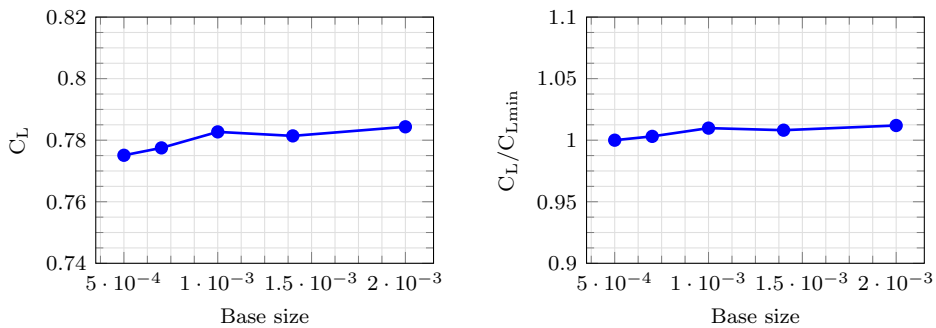
(a) Lift coefficient plotted against the smallest base size (element size) in the domain

(b) Lift coefficient for a base size divided by the lift coefficient for the smallest base size plotted against base size

Figure 16: Mesh independency study for NASA/LANGLEY LS(1)-0417 with c_f=0.25c and α_f=5°
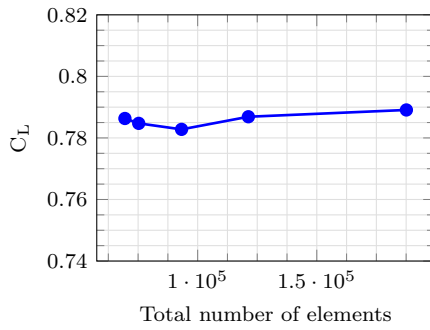
(a) Lift coefficient plotted against the total number of elements in the domain
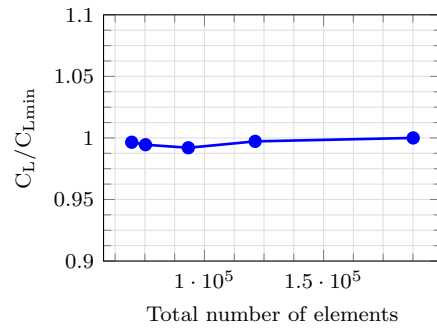
(b) Lift coefficient for total number of elements divided by the lift coefficient for the domain with most elements plotted against total number of elements in the domain

Figure 17: Domain independency study for NASA/LANGLEY LS(1)-0417 with c_f=0.25c and α_f=5°

5.3   Time-step sensitivity study, EPPLER E817

A time-step sensitivity study was performed for the EPPLER profile with $10°$ flap angle to see how the time-step would affect the solution. The basis for the time-step study was a Courant number of 10 which for the chosen mesh and velocity of 17.8 m/s is equivalent to a time-step of 0.0005 s. Three larger and one smaller time-step were tested, and the results can be seen in figure 18. It is evident that the solution is not very time-step sensitive. A time-step of 0.001 s was therefore used in the analysis as it was considered to give accurate results and have a shorter computational time than a time-step of 0.0005s. The total computational time for the steady analysis were approximately 30 minutes and the unsteady analysis could take up to three hours.
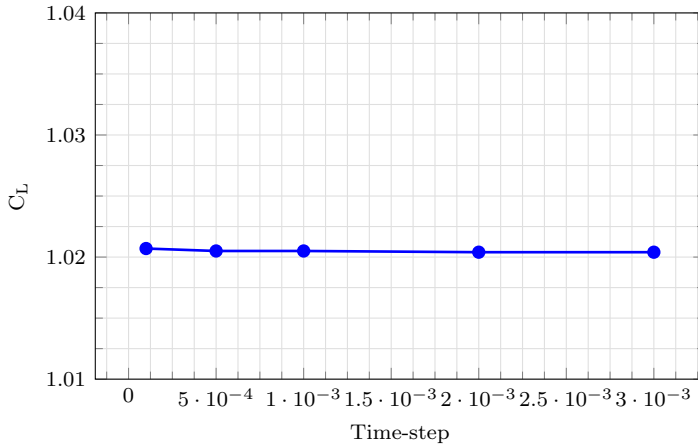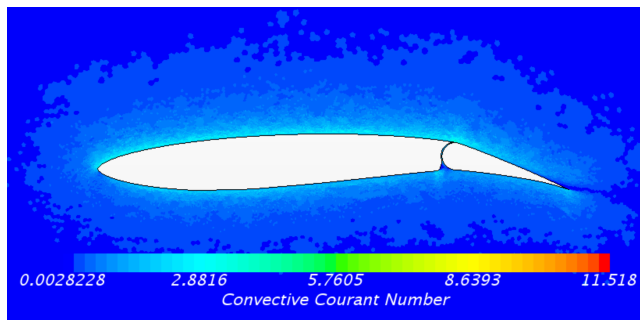

Figure 18: Time-step sensitivity study

Figure 19: Courant numbers for EPPLER E817 with c_f=0.25c, $\alpha_f = 10°$ and Δt=0.001

5.4 Law of the wall

As mentioned previously in this report it is important to satisfy the law of the wall and in this case maintain the y^+ value within the logarithmic layer. Figure 20 and 21 shows y^+ values around the EPPLER E817 and the NASA/LANGLEY LS(1)-0417 profiles with a flap angle of $0°$. Here it can be seen how the value differs along the profile due to the velocity changes. Even though there are a few y^+ values that are outside the desired logarithmic area, this distribution is considered sufficient as it would be impossible to satisfy the law of the wall at every point along the foil. When evaluating the foil profiles with larger flap angles, there is even more variation in the y^+. This is as expected due to the increase in velocity variation over the foil. There are small disturbances all along the y^+, this is probably due to some unevenness in the foil geometry made in the CAD software. If figure 15 is studied more closely one can see the unevenness in the mesh in figure 15a. Ideally the geometry should have been fixed and the analysis run again, but due to lack of time this was not possible. As the tendency in the plot is quite clear the results are considered sufficient for evaluating the flap hinge moment and the hydrodynamic forces.
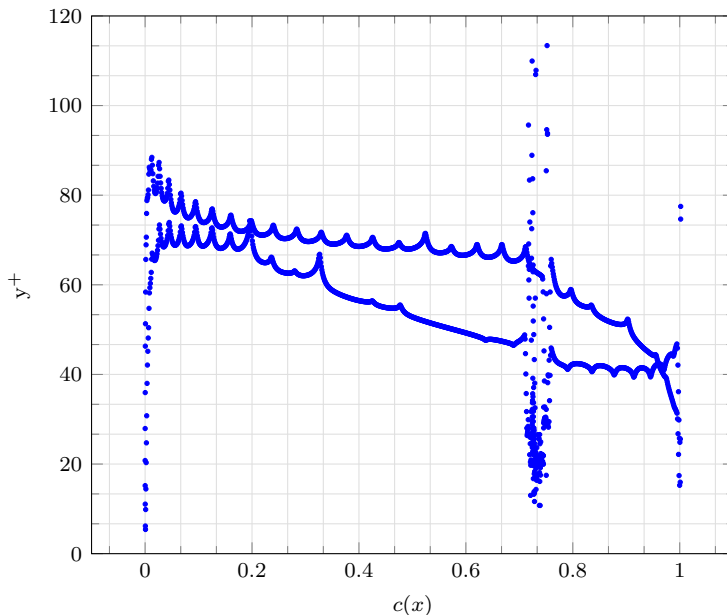

Figure 20: y^+ values for EPPLER E817 with c_f=0.25c, α=0, α_f=0 and Re=20 · 10^{-6}
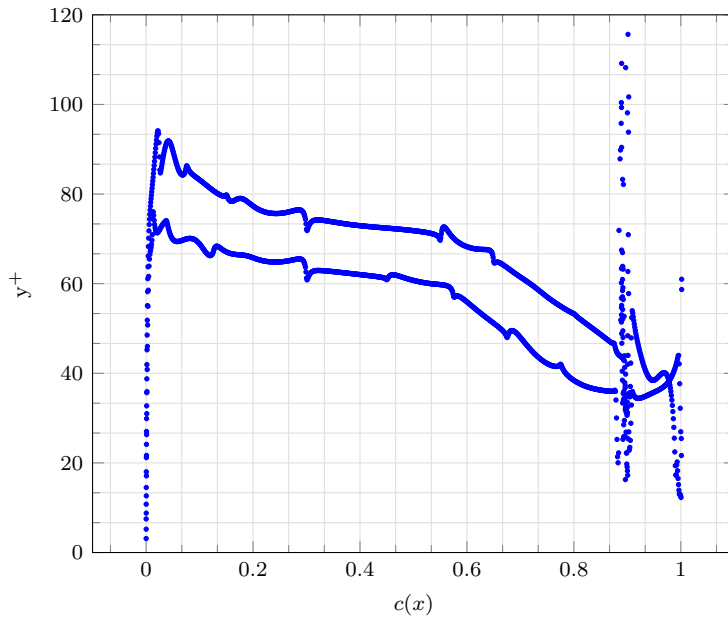
Figure 21: y^+ values for NASA/LANGLEY LS(1)-0417 with c_f=0.1c, α=0, α_f=0 and Re=$20 \cdot 10^{-6}$

6   Flow calculations in Xfoil

The foil profiles are also evaluated in Xfoil. Xfoil is a free, interactive software for analysing and designing air foils in subsonic flows. The software was developed by Mark Drela in the 1980's and has been continuously improved over the years. It is recognised worldwide, and the analysis are known to give good results for air foils. Xfoil uses panel method and a coupled boundary layer to analyse the two-dimensional flow around an air foil. In addition to analysing the flow around a given geometry, it also allows for designing an air foil determined by a pressure distribution.

Xfoil incorporates the boundary layer effects well. The boundary layer is described using a two-equation lagged dissipation integral boundary layer integration, in addition the transition is found using an e^N envelop method[9]. The pressure is found in the outer layer using potential theory and by iteration between the inner and outer flow of the displacement thickness, the effect of a boundary layer is included. An elaboration and description of this method is found in van Ingens review article *The eN method for transition prediction. Historical review of work at TU Delft*[20]. The code was developed to give fast and accurate descriptions of flow around air foils and to obtain convergence in the solution it iterates between the inner and outer flow of the boundary layer displacement thickness[15].

It is possible to retrieve most of the desired forces working on the foil from Xfoil. By default the software returns the C_p distribution along the chord length of the foil at hand when an analysis is run. The C_p plot shows two different graphs, a dashed and a solid. The solid plot represents the viscous solution and the dashed gives the inviscid solution. The difference between these two is that the viscous solution includes the effective shape of the foil due to the boundary layer[9]. In addition, other important results can be obtained such as the viscous and inviscid lift coefficient, drag and moment coefficient.

To make the results comparable to the analysis in STAR-CCM+ where the boundary layer is assumed to be fully turbulent, some adjustments must be made. When analysing a foil in Xfoil it is possible to adjust the x_{crit}, or x_{tr} as it is named in Xfoil, aft of this point the boundary layer will be analysed as fully turbulent. In addition, it is possible to adjust N_{crit} which determines the turbulence level, the smaller the N_{crit}, the higher the turbulence level will be. The turbulence level used in STAR-CCM+ is 1% and an N_{crit} of 2.6 gives a turbulence level of 1.009%. Steady

analysis are conducted for the EPPLER E817 and NASA/LANGLEY LS(1)-0417 with flap lengths of 0.1c, 0.25c and 0.4c for as many flap angles as possible. As the larger flap lengths give large changes in the flow, Xfoil would not converge for some of the flap lengths with large flap angles. This was expected as Xfoil is based on potential theory and will have difficulties when separation or similar phenomena are present[15].

7   Results and discussion

In this section the results found using STAR-CCM+ and Xfoil are presented and discussed. All the different tests are presented sectionally and a complete discussion of the results can be found at the end of this section. As mentioned the foil is tested to see which parameters must be considered and tested when designing flaps for a hydrofoil vessel. This is with regards to load and performance to finally be able to recommend an appropriate actuator. First the results for the simulations conducted for different foil geometries and flap lengths are presented. From these tests two geometries are chosen based on which are considered most appropriate to use on a hydrofoil vessel. The results found in STAR-CCM+ is then compared to the results obtained in Xfoil to evaluate the need for applying such a powerful software as STAR-CCM+. Finally, the effect of angle of attack is tested through analysis with different angles of attack and flap angles. Based on these results an evaluation of the programs will be performed and the results obtained will be used to find an actuator. It should be noted that when a hydrodynamic load is oscillating with time, it is the maximum load that is showed in the plots and the dashed vertical lines in the lift coefficient plots indicate at what flap angle the loads start to oscillate. The maximum load is shown in the plots as it is the hinge moment which is most interesting in this study and the maximum load will give the highest moment.

7.1   Flap length study

As mentioned earlier in this report the flap size will affect the total possible lift due to the effective change of camber. In addition, this will affect the drag and the hinge moment of the flap. The first analysis consider how the flap lengths affects the hydrodynamic loads and performance of the foils. Both the EPPLER E817 and the NASA/LANGLEY LS(1)-0417 are analysed with flap lengths of 0.1c, 0.25c and 0.4c. A steady or unsteady analysis was then conducted for each flap angle from $0°$ to $20°$ or $22°$ with an interval of $2°$. The lift and drag plots available for each analysis in STAR-CCM+ are evaluated to see if a steady or unsteady analysis is necessary, this differs from each flap length and foil profile. Typically, a steady state solution sufficient up to $\alpha = 10°$ and for larger flap angles an implicit unsteady solution was applied.

7.1.1   EPPLER E817

(a) C_L vs flap angle for EPPLER E817

(b) C_D vs flap angle for EPPLER E817

(c) C_M vs flap angle for EPPLER E817
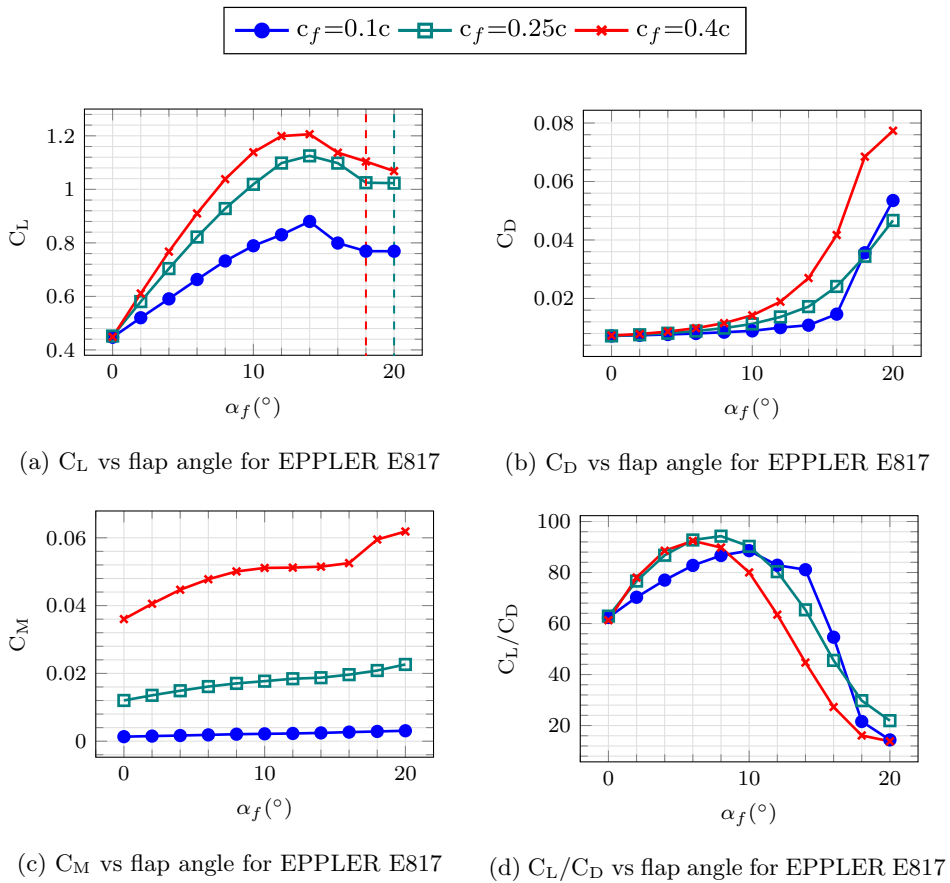

(d) C_L/C_D vs flap angle for EPPLER E817
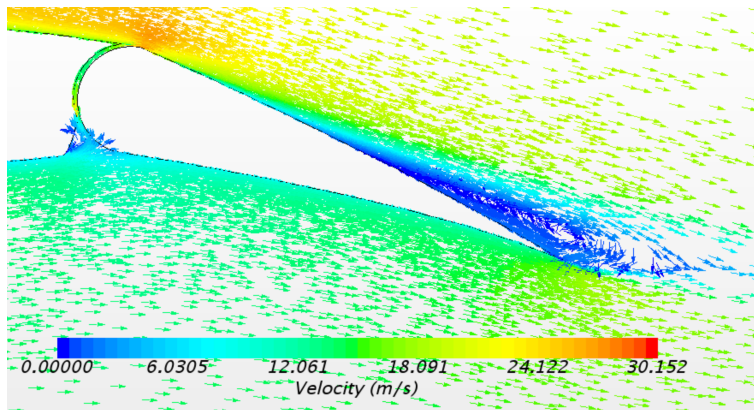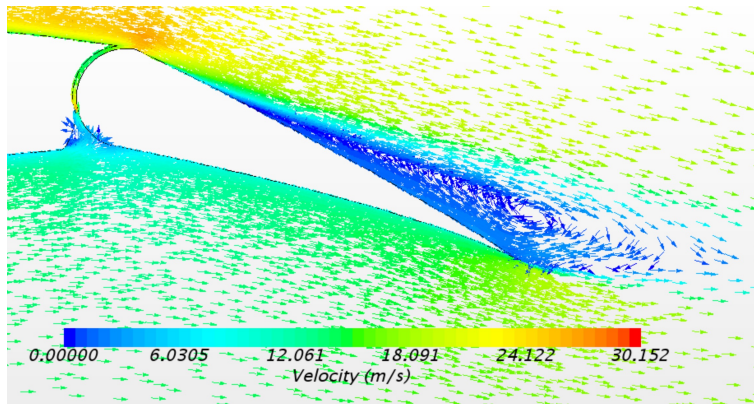
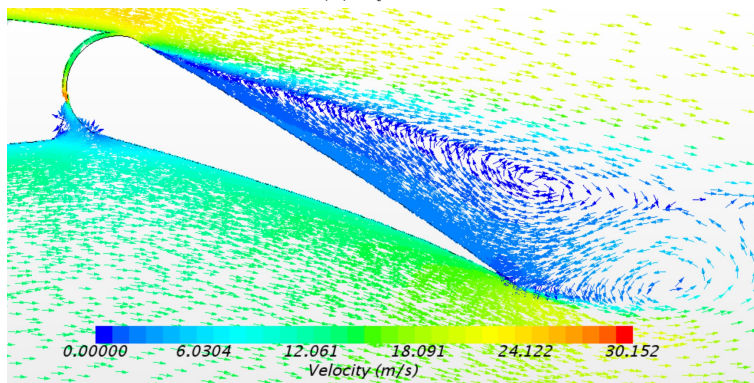Figure 22: Results for flap length study of EPPLER E817

(a) $\alpha_f = 14°$

(b) $\alpha_f = 16°$

(c) $\alpha_f = 20°$

Figure 23: Velocity vector field for EPPLER E817 with c_f=0.25c at Re=20·10^6 and $\alpha = 0°$

The results from the analysis for the EPPLER E817 profile are shown in figures 22 and 23. From the plots it is evident that a flap is very effective for increasing the maximum possible lift, without changing the angle of attack. Further this profile behaves as expected, there is a steady increase of lift with increasing flap angle until a maximum lift is reached. At this point separation occurs close to the flap hinge as seen in figure 23, this is the case for all the flap lengths and the maximum lift occurs approximately at $\alpha_f = 14°$ for all. Separation occurs because the flow is no longer able to follow the foil profile, this causes a vortex to form in this area and the pressure on the suction side increases. Hence the pressure difference over the foil decreases and so does the lift. When the flap angle is increased further to $20°$ a second vortex with opposite direction is created, which leads the hydrodynamic forces to oscillate due to the vortex shedding. This is not a desired behaviour in flying condition and should be avoided. This should not be an issue as it should not be necessary to deflect the flap more than $\approx 14°$. The maximum lift increases with increasing flap length, but so does the drag and hinge moment. The best option seems to be a flap length of 25%, where there is a reasonable amount of increased lift and it gives the best lift-to-drag ratio of the options analysed. Of course if the maximum lift for a foil with flap length of 0.25c is not sufficient, it should be considered if the increase in hinge moment is acceptable in order to gain some more lift.

7.1.2   NASA/LANGLEY LS(1)-0417

(a) C_L vs flap angle in degrees for NASA/LANGLEY LS(1)-0417

(b) C_D vs flap angle in degrees for NASA/LANGLEY LS(1)-0417

(c) C_M vs flap angle for NASA/LANGLEY LS(1)-0417

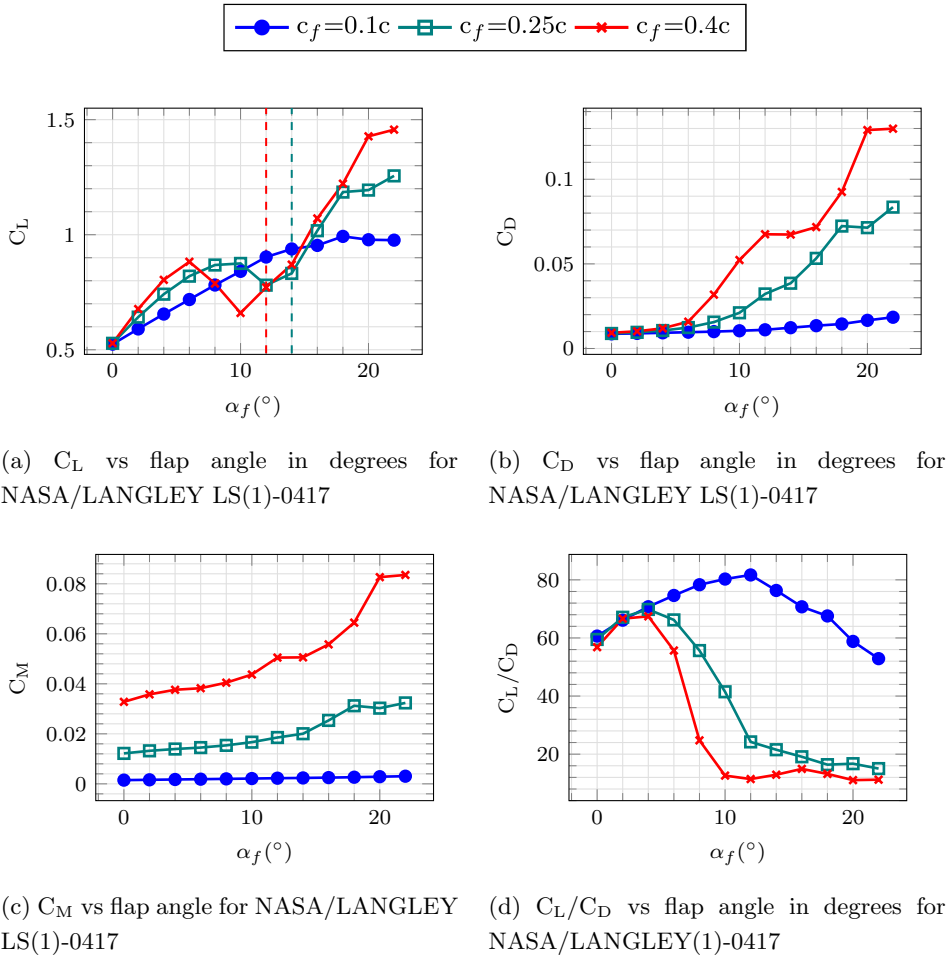(d) C_L/C_D vs flap angle in degrees for NASA/LANGLEY(1)-0417

Figure 24: Results for flap length study of NASA/LANGLEY LS(1)-0417

The NASA/LANGLEY LS(1)-0417 profile does not illustrate the same clarity in lift improvement when a flap is applied, this is not unexpected due to the shape of the foil. The foil is thick very close to the trailing edge and introducing a flap with angle will make the transition to the thinner part even more abrupt and lead to flow separation.

For the smallest flap the lift is monotonically increasing with increasing flap angle before it stagnates around $\alpha_f \approx 18°$, here a vortex starts to form already around $\alpha_f = 16°$ but this does not affect the hydrodynamic loads significantly and the hinge moment is almost independent of the flap angle. When the flap length is increased, a different behaviour can be noticed. Already at a flap angle of 12° the flow around the foil with a flap length of 0.25c separates at the junction between the wing and the flap. This leads to a sudden drop in lift, but this does not affect the hinge moment which is steadily increasing for increasing flap angle. Still applying the larger flap lengths to control lift might not be recommended as the hydrodynamic loads and response can be unpredictable.

When the lift drops due to the vortex generation the maximum lift increases again when the flap angle is further increased. This can be explained by looking at figure 26 where the pressure distribution for the NASA/LANGLEY LS(1)-0417 profile with a flap length of 0.25c is shown. At $\alpha_f = 12°$ the vortex is established and the pressure at the suction side increases. When the flap is deflected further the pressure on the pressure side increases and the suction side decreases again, due to the formation of the vortex with opposite direction as seen in figure 25c. The hydrodynamic loads are oscillating at this stage, making it inappropriate for stabilisation of a hydrofoil vessel at flight. What is interesting with this behaviour is that the hinge moment is not greatly affected by the oscillations and the maximum moment keeps increasing steadily with increasing lift, the oscillating loads are more damaging to the lift-to-drag ratio as the drag is greatly increased by the vortex generation.
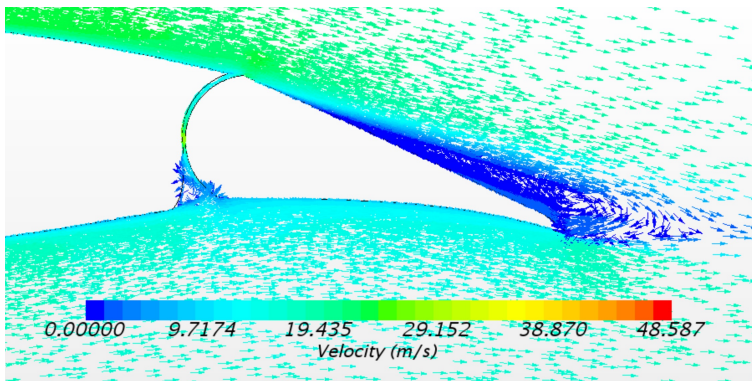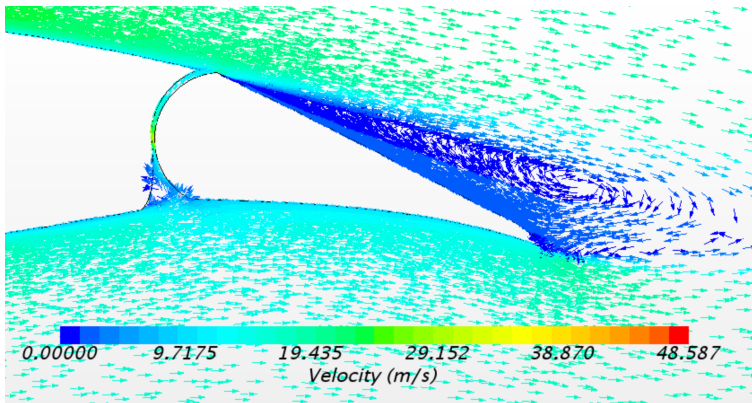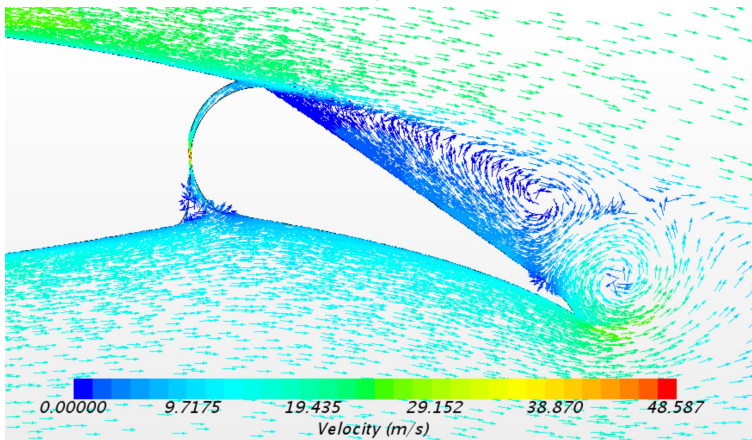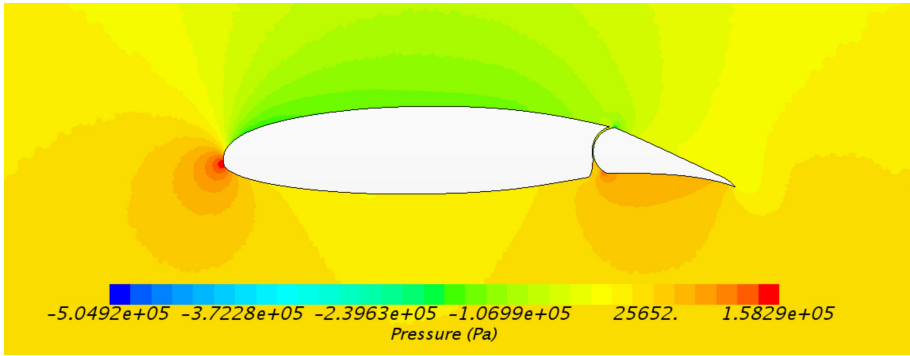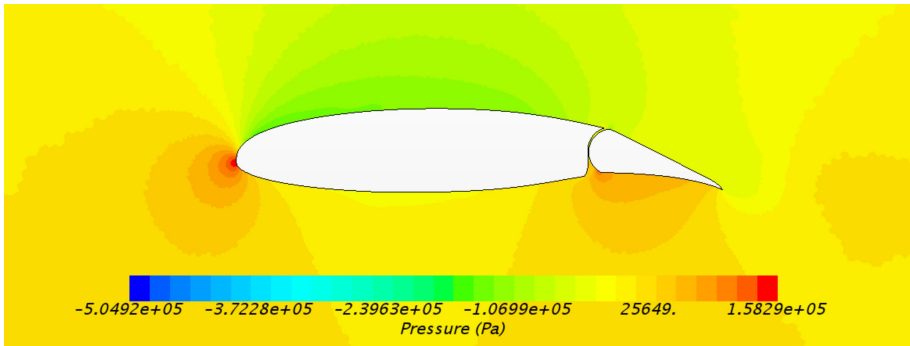
(a) $\alpha_f = 10°$
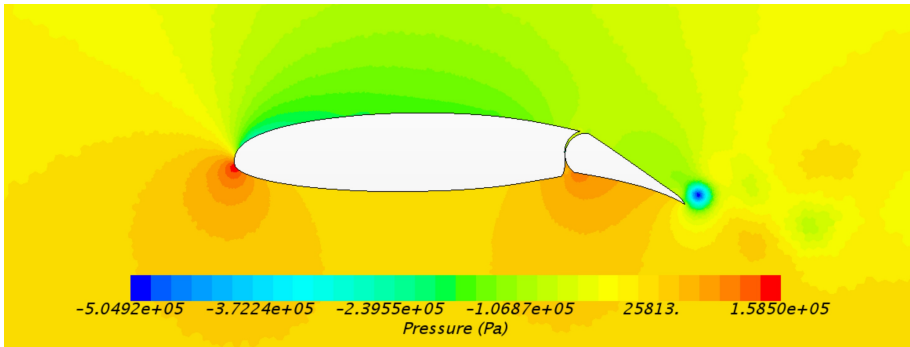

(b) $\alpha_f = 12°$

(c) $\alpha_f = 20°$

Figure 25:   Velocity vector plot with separation on the flap hinge for NASA/LANGLEY LS(1)-0417 with c_f=0.25c

(a) and $\alpha_f = 10°$

(b) $\alpha_f = 12°$

(c) $\alpha_f = 20°$

Figure 26:   Pressure scalar plot with separation on the flap hinge for NASA/LANGLEY LS(1)-0417 with c_f=0.25c

7.1.3   Foil Theory

As no formulation for estimating the hinge moment using foil theory was found, only the equation for the lift coefficient introduced in section 3.1.2 is plotted for different flap lengths and flap angles in figure 27. This equation only considers the length of the flap and angle, and the shape of the foil has no influence on the lift. It can therefore not be expected to give accurate results for any of the geometries analysed in this report. Nevertheless, it gives an understanding of the effect of the flap and an indication of the dimension of the lift, and this results in a decent approximation to the effect of the flap for all c_f for the EPPLER E817 and for c_f=0.1c for the NASA/LANGLEY(1)-0417 profile. Unfortunately, it is not very informative with regards to the size of the moment the flap hinge will be exposed to.
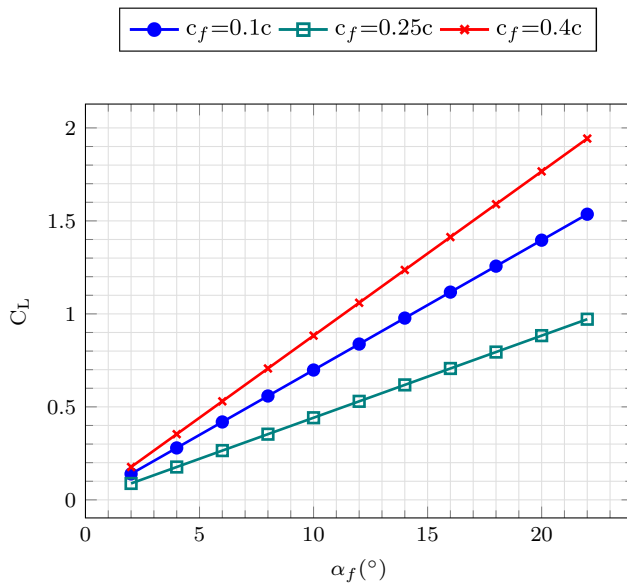

Figure 27: Lift coefficient for a foil with flap found by linear foil theory

7.1.4   Summary

Evaluating the results in this section it is seen that the lifting capability of both foil profiles are improved when flaps are applied, as long as the flap length is appropriate with regards to the flap geometry. For the NASA/LANGLEY LS(1)-0417 the most appropriate flap length is around 0.10c as this will result in the junction between the wing and the flap being located at the thinner part of the profile. Using this flap is still quite efficient as the lift coefficient is almost doubled without any unwanted separation or vortex shedding occurring, and the hinge moment is relatively small. For the EPPLER E817 profile all the flap lengths give reasonable results where c_f=0.25c has the best lift-to-drag ratio and the hinge moment is much less than for c_f=0.4c. The hydrodynamic loads do not start to oscillate before $\alpha_f = 20°$ which makes it reliable with regards to predicting the hydrodynamic behaviour. Based on this, a flap length of 0.25c is chosen for the EPPLER E817 profile and a flap length of 0.1c is chosen for the NASA/LANGLEY LS(1)-0417 profile.

7.2   Xfoil vs STAR-CCM+

As experimental validation was not available it was interesting to compare the results obtained in STAR-CCM+ with another software applying a different method. The foil geometries were therefore also analysed in Xfoil, with flap lengths of 0.1c, 0.25c and 0.4c. As Xfoil is based on potential and boundary layer theory, rotationfree flow is assumed and the vortex generation will not be accounted for. Also, Xfoil does not include viscous effects directly but uses boundary layer theory and the displacement thickness to include boundary layer effects. This leads to some difficulties in applying Xfoil when the foils have long flaps at large flap angles, as separation is prominent under such circumstances.
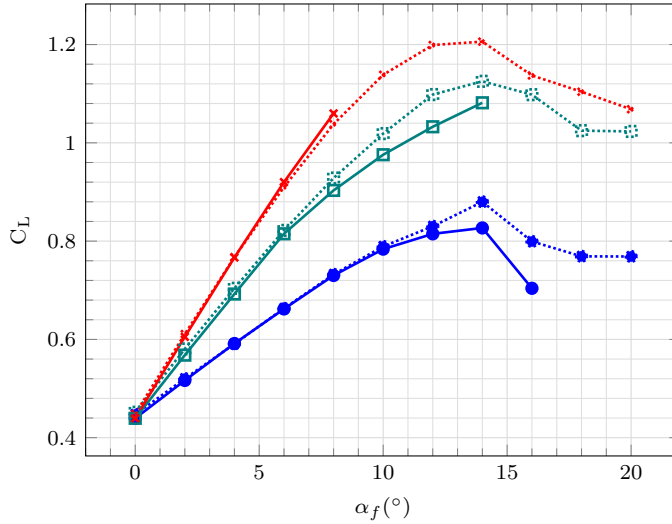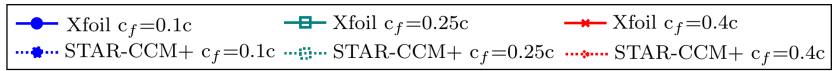
7.2.1   EPPLER E817

In figure 28 the results obtained from Xfoil and STAR-CCM+ are shown. Unfortunately, Xfoil would not converge and give an indication of the loads for many of the flap lengths and angles, this is as mentioned due to the fact that Xfoil is based on potential theory. Disregarding this and looking at the results obtained before separation occurs, the results are in quite good compliance. The lift generated on the hydrofoils are almost identical for the two software, this shows that potential theory and N-S solutions are both good tools as long as they are used within their limits.

Looking at the hinge moment the percentual difference between the moment obtained by STAR-CCM+ and Xfoil is quite large. The fact that Xfoil does not properly account for the viscous effects might affect the calculated pressure distribution, that again affects the estimated loads. The difference is dramatically reduced with increasing flap length, this might be because in Xfoil the flap is fully attached to the wing. In STAR-CCM+ there is a small gap between the wing and the flap that allows some fluid to flow through. The effect of this cap might be reduced for the increasing flap length as other effects become more dominant.

The Cp distribution is also of great interest when evaluating foil performance. In figure 29 the Cp distribution for EPPLER E817 as found in STAR-CCM+ and Xfoil is presented, there is some disagreement between the plots. In addition, there are some disturbances in the STAR-CCM+ analysis, this is probably due to some unevenness in the geometry imported from the CAD software as mentioned in section 5.4. It is the pressure difference between the suction and pressure side that gives the estimated lift on the foil. The pressure distribution from Xfoil is shifted

in the same direction on both sides, so the total difference might therefore not be that big, and still result in correct calculation of the lift. Looking at the flap on the EPPLER E817 profile the pressure distribution found in Xfoil is shifted towards each other, reducing the lift on the flap, and hence reducing the estimated hinge moment as seen in figure 29.
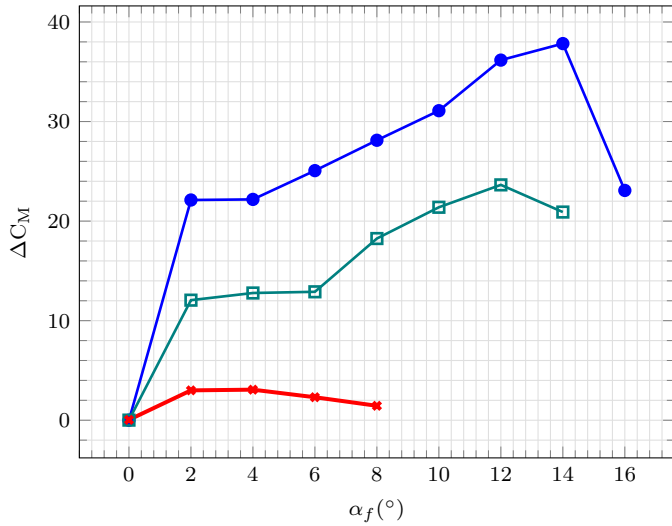
(a) Lift coefficient vs flap angle for EPPLER E817

(b) ΔC_M vs flap angle for EPPLER E817

Figure 28: Results from Xfoil and STAR-CCM+ for the EPPLER E817 with c_f=0.1c, c_f=0.25c and c_f=0.4c and $\alpha_f = 0° - 20°$. Here $\Delta C_M = \frac{C_{M,STAR} - C_{M,Xfoil}}{C_{M,STAR}} \cdot 100$
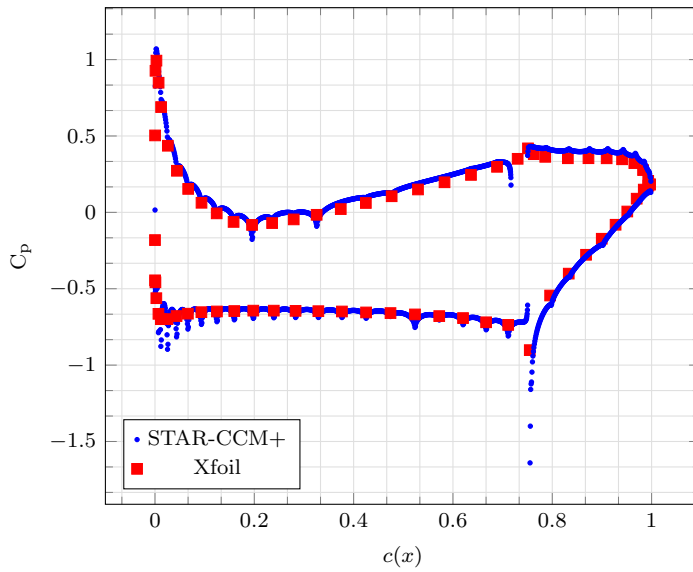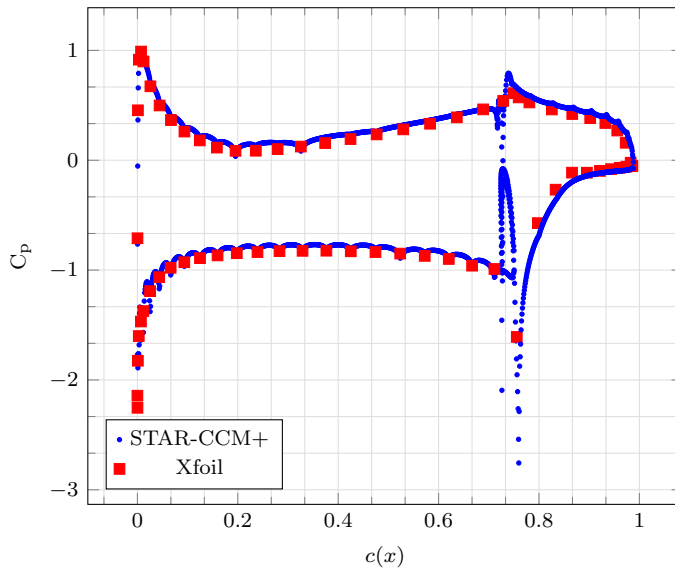
(a) $\alpha_f = 5°$

(b) $\alpha_f = 14°$

Figure 29: C_p vs chord length from STAR-CCM+ and Xfoil for EPPLER E817 with c_f=0.25c

7.2.2   NASA/LANGLEY LS(1)-0417

For the NASA/LANGLEY(1)-0417 profile there is more disparity in the results. For c_f=0.1c the software gives similar lift coefficient but there are large deviations in the moment coefficient. For c_f=0.25c and c_f=0.4c on the other hand there is not much agreement in any of the calculated loads. This can again be related to the pressure distribution found by Xfoil. Comparing it with the results from STAR-CCM+ for a foil with flap length of 0.25c there is a large difference in the pressure distribution. The difference between the suction and pressure side is much larger for the pressure distribution found in Xfoil, and this leads to a higher estimated lift coefficient. Also, the pressure distribution over the flap is very different from the one calculated in STAR-CCM+ resulting in a large deviation between the results.

Xfoil is not able to account for the flow separation found in STAR-CCM+ for the foils with flap length of 0.25c and 0.4c. This is because Xfoil assumes that the boundary layer is thin and applies the assumptions and simplifications mentioned in section 3.3. As a result, Xfoil will in many cases estimate separation to occur later than what is the case.
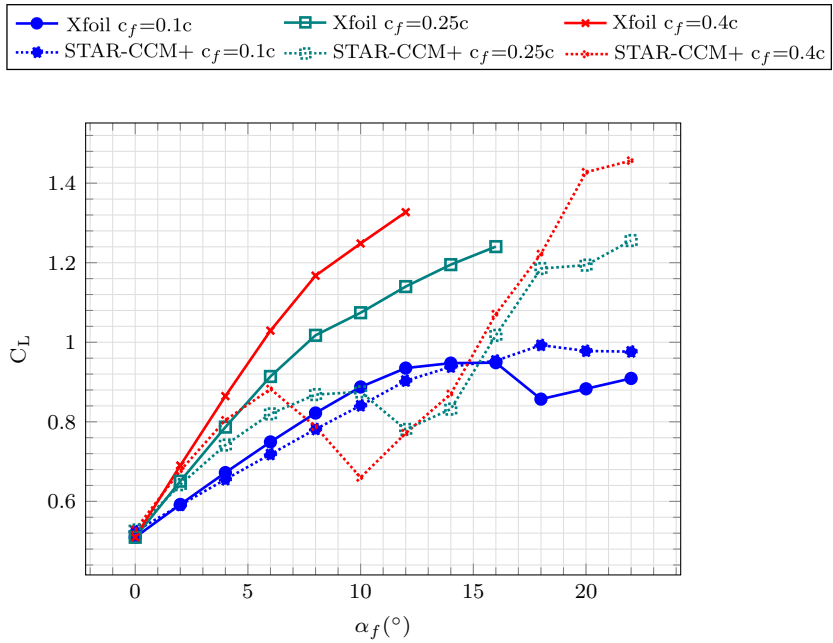
(a) Lift coefficient vs flap angle for NASA/LANGLEY LS(1)-0417
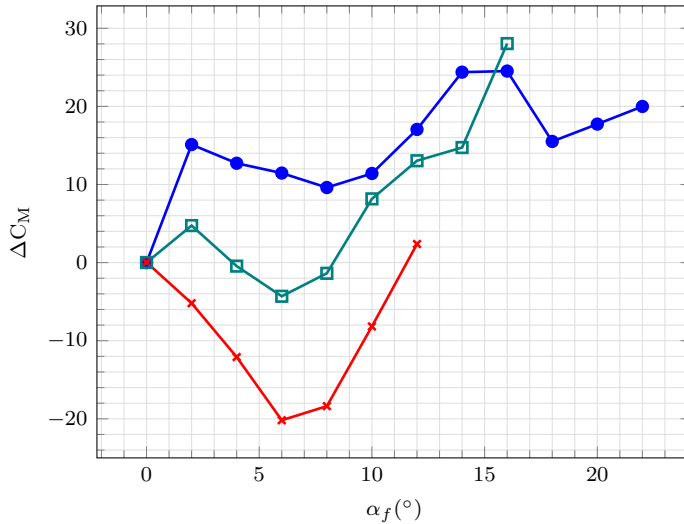
(b) ΔC_M vs flap angle for NASA/LANGLEY LS(1)-0417

Figure 30:   Results from Xfoil and STAR-CCM+ for the NASA/LANGLEY LS(1)-0417 with c_f=0.1c, c_f=0.25c and c_f=0.4c and α_f = $0° - 20°$.   Here $\Delta C_M = \frac{C_{M,STAR} - C_{M,Xfoil}}{C_{M,STAR}} \cdot 100$

(a) c_f=0.10c and $\alpha_f = 5°$
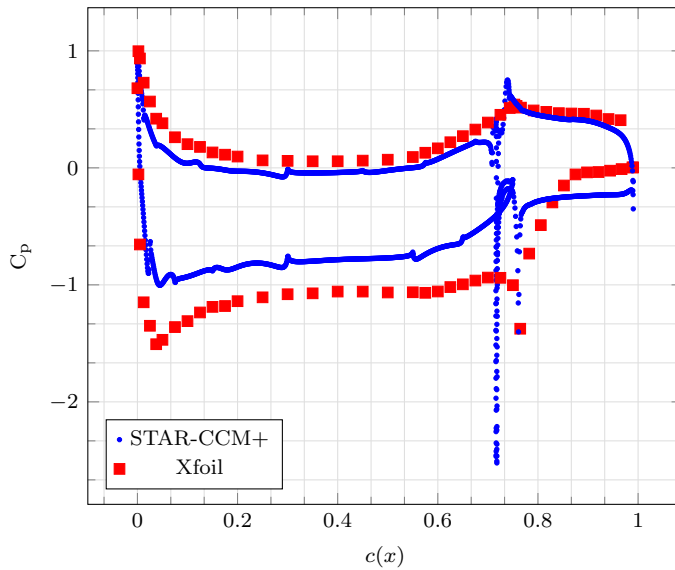
(b) c_f=0.25c and $\alpha_f = 12°$

Figure 31: C_p vs chord length from STAR-CCM+ and Xfoil for NASA/LANGLEY LS(1)-0417

7.2.3   Summary

The comparison between the two software show good results for lift calculation, but it also reveals some of the uncertainties related to the use of computer-based software for estimating hydrodynamic loads. As mentioned Xfoil assumes the boundary layer to be thin and therefore wrongly estimates the time of separation. On the other hand, STAR-CCM+ assumes the boundary layer to be fully turbulent, which is not always the case. Here Xfoil has the possibility of applying a good laminar to turbulent transition that give results for estimating hydrodynamic loads on foils. Another issue that differs the two software is the possibility manipulating the foil geometry. In Xfoil the flap is fully attached to the flap without any gap between the wing and the foil. STAR-CCM+ allows for a more realistic representation of the geometry and includes the flow that will pass between the wing and the flap. This flow will probably affect a foil with a small flap sizes more than a foil with a large flap size.

7.3   Effect of angle of attack

From the literature study it is known that for air foils an increased angle of attack reduces the effectiveness of the flap. In this section the results from analysis where both angle of attack and flap angle were present are presented. To determine how the flap effectiveness is affected by the angle of attack a plot for ΔC is presented. Here ΔC is the lift coefficient for an angle of attack with the given flap angle minus the lift coefficient with the same angle of attack but with zero flap angle. This is to isolate the effect of the flap making it easier to compare the flap effectiveness for the different angles of attack.

7.3.1   EPPLER E817
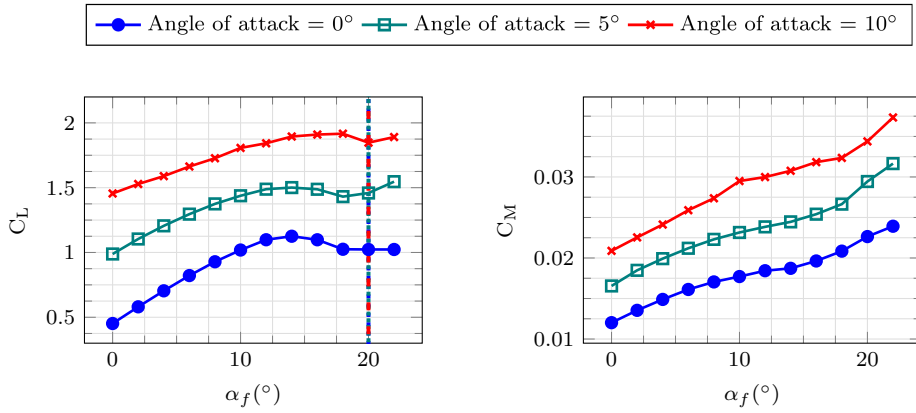
(a) Lift coefficient vs flap angle for EP-PLER E817 at different angles of attack

(b) Moment coefficient vs flap angle for EP-PLER E817 at different angles of attack
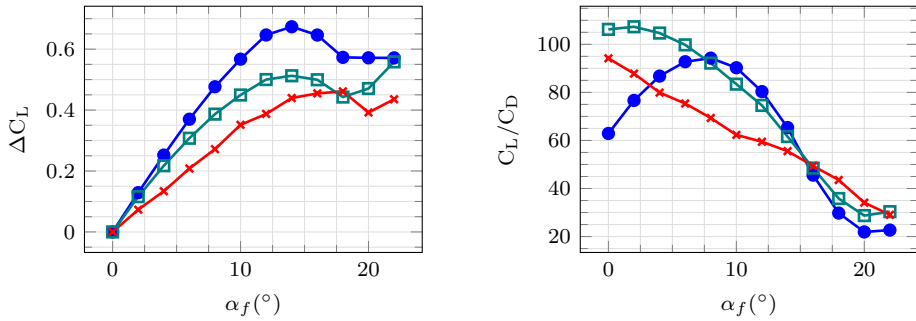
(c) $\Delta C_L = C_L(\alpha_{fi}) - C_L(\alpha_{f0})$ vs flap angle for EPPLER E817 at different angles of attack

(d) Lift to drag ratio vs flap angle for EP-PLER E817 at different angles of attack

Figure 32: Results from analysis in STAR-CCM+ for EPPLER E817 with c_f=0.25c for flap angles at different angles of attack

7.3.2   NASA/LANGLEY LS(1)-0417
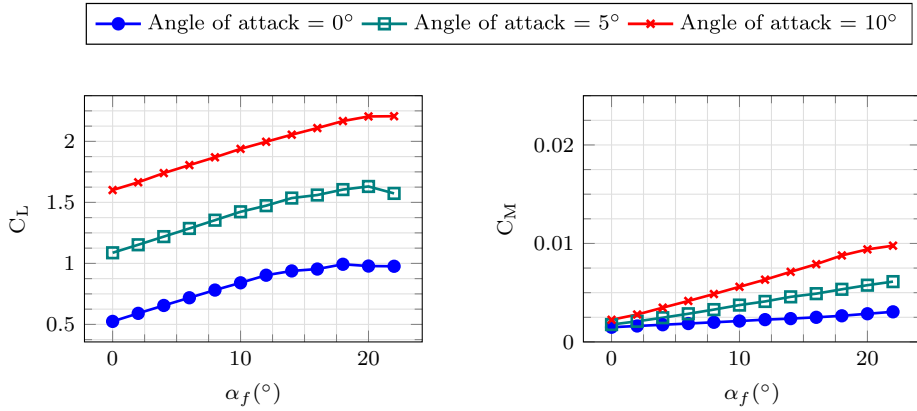
(a) Lift coefficient vs flap angle for NASA/LANGLEY LS(1)-0417 at different angles of attack

(b) Moment coefficient vs flap angle for NASA/LANGLEY LA(1)-0417 at different angles of attack
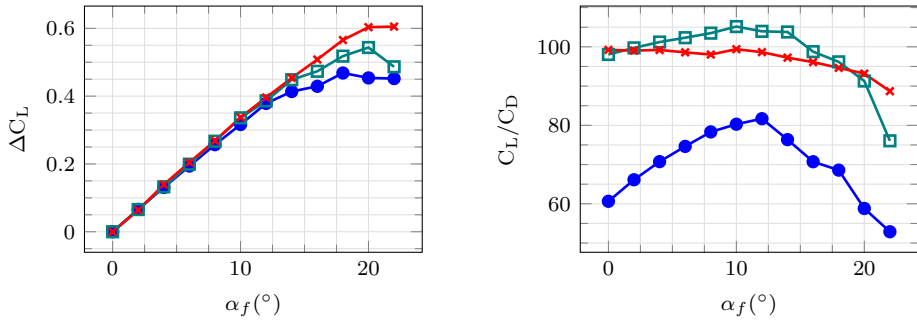
(c) $\Delta C_L = C_L(\alpha_{fi}) - C_L(\alpha_{f0})$ vs flap angle for NASA/LANGLEY LS(1)-0417 at different angles of attack

(d) Lift to drag ratio vs flap angle for NASA/LANGLEY LA(1)-0417 at different angles of attack

Figure 33: Results from analysis in STAR-CCM+ for NASA/LANGLEY LS(1)-0417 with c_f=0.10c for flap angles at different angles of attack

7.3.3 Summary

The effect of the flap on the EPPLER E817 profile is greatly reduced by increasing the angle of attack. This not the case for the NASA/LANGLEY LS(1)-0417 profile which is almost unaffected by the angle of attack. Actually, the effect of the flap angle increases for larger angles of attack when the flap angle is large, as seen in figure 33c. This is probably due to the size of the flaps compared to the total chord length, and the thickness at the flap hinge compared to maximum thickness. The EPPLER E817 profile has significantly larger flap size and the thickness at the flap hinge is much greater than for the NASA/LANGLEY LS(1)-0417 where the flap only is 10% of the total chord length and the thickness at the hinge is relatively small compared to the maximum thickness of the foil.

7.4 General discussion

Comparing the two foil profiles analysed in this study, there are pros and cons for both geometries. The EPPLER E817 profile is designed for operating as a hydrofoil and it can be seen in figure 29 that it has a more even pressure distribution than the NASA/LANGLEY LS(1)-0417 profile, even when it has a longer flap. The hydrofoil profiles are designed to have an even pressure distribution in order to avoid pressure peaks that can lead to cavitation. Despite this the NASA/LANGLEY LS(1)-0417 profile gives very good results. As the small flap applied gives a small moment on the hinge in addition to increasing the maximum lift reasonably, which is desirable with regards to minimizing the size of the actuator. These good results might be due to the fact that the NASA/LANGLEY LS(1)-0417 profile is design to operate as an air foil, and flaps are more commonly used on air foils than on hydrofoils. This is also reflected by the greatly improved lift-to-drag ratio for the NASA/LANGLEY LS(1)-0417 profile with increasing angle of attack. As aircrafts are dependent on a good performance during take-off and landing. Which foil profile would be the most appropriate to apply will therefor depend on the maximum lift required and how efficient and economical the hydrofoil vessel must be.

8   Actuator

8.1   Theory and method

An actuator is a component which controls a motion or mechanism in a system and can either have linear or rotary motions. It converts energy into mechanical motion by an electrical current, pneumatic pressure or hydraulic fluid pressure using a control system. A hydraulic actuator is considered appropriate to control the flaps on a hydrofoil vessel as it is powerful and reliable, and aircrafts often use this to control their systems[28]. In addition, hydraulic actuators can have strokes as long as necessary and the power supply can be placed far away from the actual actuator. Even though hydraulic actuators are considered safe, precaution must be taken in regard to the high pressure present in such a system, and that there always will be a risk of leakage that may cause failure of the system[14]. The actuator considered in this thesis is based on the components made available by *Servi Group*[6].

The force available in an actuator can be simplified to give an estimate of the necessary size of the component. An illustration of a hydraulic- cylinder and valve working principle is shown in figure 34. Here the cylinder force can be expressed as in equation 25 if no losses are considered, here P_i is the chamber pressure[14].

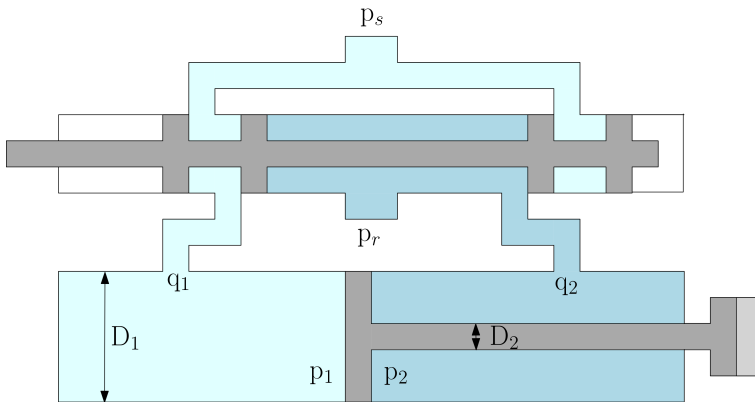$$F_c = p_1 \pi \frac{D_1^2}{4} - p_2 \pi \frac{(D_1^2 - D_2^2)}{4} \tag{25}$$

Figure 34: Sketch of hydraulic actuator working principle

Using actuators on hydrofoil vessels is not as convenient as on aircrafts, there are

difficulties related to where to mount them with regards to space and minimizing how they affect the flow. One possibility might be to attach an arm to the hinge inside the flap and add a hydraulic actuator inside the wing to control the angle. This might be difficult as the forces working on the hinge might be so large that an actuator will not fit inside the wing. Another option is to mount the actuator on the pressure side of the foil as demonstrated in figure 35. The disadvantage with this is that the component will disturb the flow around the foil in the area where it is installed and increase the drag. If this design is used it is necessary to include the arm that works from the flap hinge to the piston arm on the actuator. For a hydrofoil of maximum thickness of about 11% of the chord length and a flap length of 25% this arm may be approximately 10cm.
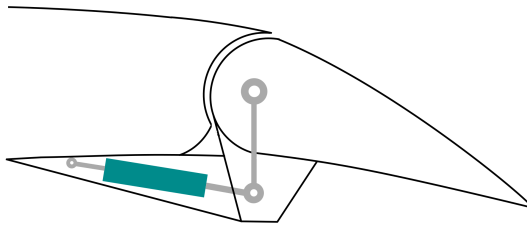

Figure 35: Sketch of flap with hydraulic actuator (not to scale)

As mentioned the products made available by Servi Group will be used as a basis for recommending actuators for the foils. Some simplifications are made in these calculations as the design is not final and small angles and distances are assumed to be legible, it is also assumed that the force is working 90° on the actuator arm. The calculations will be based on the concept of a simple cylinder with a piston where the design pressure and effective piston area (A) will decide the dimensions of the actuators. To find the effective area of the cylinder the area occupied by the rod must be subtracted from the piston area before it can be multiplied by the design pressure.

First the desired stroke length will be found using the simple geometry in figure 36a and equation 26. Then the necessary effective piston area is estimated based on the force caused by the hinge moment and design pressure, before the table for standard cylinder dimensions seen in appendix B is used to find a model that meets the demands for the system based on equation 28. This will give an estimate of the dimensions of a hydraulic actuator that can be used to control the flaps on the submerged foil system.

$$S_{\text{cylinder}} = a_{\text{actuator}} \cdot \tan(\alpha_f) \tag{26}$$

$$A = \frac{F_c}{P_d} \tag{27}$$

$$\frac{\pi}{4}(D_1^2 - D_2^2) = A \tag{28}$$
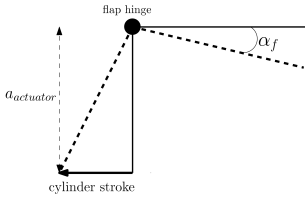
(a) Geometry used for estimating necessary cylinder stroke length
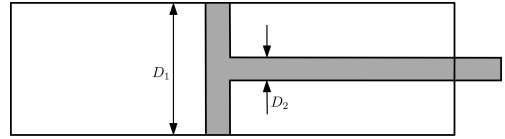
(b) Simple cylinder sketch

Figure 36: Geometry used for estimating cylinder dimensions

8.2   Adaptation of actuator

After the evaluation of the different foil and flap geometries it is decided to find appropriate actuators for the EPPLER E817 profile with flap length of 0.25c, and NASA/LANGLEY LS(1)-0417 with flap length of 0.1c. The situations considered as critical based on previous sections is both foils with an angle of attack of 10° and a flap angle of 18°. The critical angle of attack of 10° is used based on discussions with the co-supervisor. Where the conclusion was that this is far beyond any angle of attack the hydrofoil will experience. To obtain the critical loads for these geometries the analysis are run again with salt water properties as shown in table 3. The results from these analysis can be seen in table 4.

Table 3: Parameters used for finding maximum moment

c	1 m
$c_{f,\text{EPPLER E817}}$	0.25c
$c_{f,\text{NASA/LANGLEY}}$	0.1c
s_f	2x4 m
ρ_{sea}	1025 kg/m^3
ν_{sea}	1.346·10^{-3} Pa·s
$a_{actuator}$	100 mm
U	18 m/s

Table 4: Maximum flap hinge loads from STAR-CCM+

	C_M	M_{2D}	M_{TOT}	F_{actuator}
EPPLER E817	0.03411	5633 Nm/m	22532 Nm	225320 N
NASA/LANGLEY LS(1)-0417	0.00907	1433 Nm/m	5732 Nm	57320 N

The foil system is assumed to have a total span of 10 meters with two individual foils with a span of 5 meters each, here each foil has a flap with a span of 4 meters. In the previous section it is seen that a flap deflection of 14° gives an effective increase in lift for both foil profiles, so an actuator capable of deflecting the flap to 18° is considered appropriate. Further deflection of the flap will result in unwanted effects such as oscillation of the loads. This results in a necessary cylinder stroke of 32mm, given that the distance between the flap hinge and actuator arm is 100mm. The moments in table 4 are the maximum loads in steady state. As the system will be dynamic and the desired motion velocity of the cylinder arm is uncertain, a safety factor of 1.5 is multiplied with the load[40]. From the Servi AS product catalogue it can be read that the hydraulic cylinders have a design pressure of 250 bar, the diameter of the cylinder will be based on this design pressure.

For the EPPER E817 profile the actuator will have to withstand a force of approximately 338kN when a safety factor of 1.5 is included. This requires an effective area of ≈17000mm^2 given a design pressure of 250bar. An alternative is then to use a cylinder with piston diameter of 160mm and a rod diameter of 80mm as found in the Servi CD25 standard cylinder catalogue. This cylinder has a length of a little

more than 420mm and an outer diameter of 185mm. For the NASA/LANGLEY LS(1)-0417 profile the actuator has to withstand a force of 86kN when a safety factor of 1.5 is included. This requires an effective area of $\approx 3440\text{mm}^2$. From the catalogue for standard cylinders there is an appropriate option that has a piston diameter of 80mm and a rod diameter of 40mm, with a length of approximately 240mm. The actuator on the EPPLER E817 profile will occupy almost half the chord length of the foil. A more thorough analysis of the flow around the foil with an actuator attached could be conducted to investigate whether it would be more efficient to apply two smaller actuators. In this evaluation one actuator per foil is considered sufficient, assuming a single cylinder can provide the required reliability. This is given that the material and construction of the hydrofoil is able withstand the force in only one point, without deforming due to uneven load distribution. If the material is too weak the possibility of applying two or three actuators on each foil should be considered.

9   Concluding remarks

This thesis has investigated different methods for estimating the hydrodynamic loads on two foil profiles with a trailing edge flap. The CFD software STAR-CCM+ and Xfoil are tested for different flap lengths resulting in different flow characteristics. Xfoil has proven to be a reliable tool for calculating the lift in flows with limited viscous effects and can account for some degree of flow separation. When considering the flap hinge moment Xfoil proved to be insufficient, and it is recommended to apply a more advanced program when this is evaluated. STAR-CCM+ is considered a useful tool for the simple cases evaluated in the thesis. However, the experience from this thesis is that the use of Xfoil is more efficient, as it is faster, simpler and gives sufficient quality results in the majority of cases tested, disregarding the hinge moment. Still it is important to keep in mind the limitations of using potential theory, and apply more powerful tools if the circumstances are uncertain. Even though STAR-CCM+ is a user-friendly software with a good interface not all the solutions are intuitive, and it might be difficult to solve potential problems due to insufficient feedback in the error messages.

The goal of the thesis was to recommend an appropriate actuator for a foil with flap, this was done for two potential foil geometries. For a foil with chord length of one meter and a Reynolds number of $20 \cdot 10^6$ two actuators of outer diameter 95mm and 145mm with approximate lengths of 240mm and 355mm are recommended. These are considered appropriate as they will fit underneath the foil and not unnecessarily disturb the flow.

10   Further work

It would be recommended to perform some dynamic analysis to see if this increases the load on the hinge. Further it would be interesting to do experimental tests to be able to compare with the results found using the software. Also, a more thorough study of the pressure distribution would be necessary to investigate if cavitation might be an issue for the foil profiles when a flap is applied. Another aspect that should be investigated is the alternative to applying a hydraulic cylinder, other solutions might be more appropriate. Also, the structure of the actuator is not thoroughly investigated and a detailed study of this aspect would be recommended to obtain a more reliable solution.

References

[1] Courant Friedrichs Lewy condition. https://www.cfd-online.com/Wiki/Courant%E2%80%93Friedrichs%E2%80%93Lewy_condition.

[2] EPPLER 817 HYDROFOIL AIRFOIL (e817-il). http://airfoiltools.com/airfoil/details?airfoil=e817-il.

[3] K-epsilon models – CFD-Wiki, the free CFD reference. https://www.cfd-online.com/Wiki/K-epsilon_models.

[4] K-omega models – CFD-Wiki, the free CFD reference. https://www.cfd-online.com/Wiki/K-omega_models.

[5] NASA/LANGLEY LS(1)-0417. http://airfoiltools.com/airfoil/details?airfoil=ls417-il.

[6] Servi group. https://www.servi.no/hydraulikk/hydraulikk-sylinder.html.

[7] SST k-omega model – CFD-Wiki, the free CFD reference. https://www.cfd-online.com/Wiki/SST_k-omega_model.

[8] Two equation turbulence models – CFD-Wiki, the free CFD reference. https://www.cfd-online.com/Wiki/Two_equation_turbulence_models.

[9] Xfoil subsonic airfoil development system. http://web.mit.edu/drela/Public/web/xfoil/.

[10] J. D. Anderson. Ludwig Prandtl's Boundary Layer. *Physics Today*, 58(12)(December):42–48, 2005.

[11] Y. A. Cengel, J. M. Cimbala, and M. Kanoglu. *Fluid Mechanics Fundamentals and Applications*. Mc Graw Hill Higher Education, 2nd edition, 2010.

[12] L. L. Erickson. *NASA Technicl Paper 2995, Panel Methods - An Introduction*. NASA - National Aeronautics and Space Administration, Moffett Field, California, 1990.

[13] O. M. Faltinsen. *Hydrodynamics of High Speed Marine Vehicles*. Cambridge University Press, 2005.

[14] O. Gomis-Bellmunt and L. F. Campanile. *Design Rules for Actuators in Active Mechanical Systems*. Springer, London, 2010.

[15] O. Günel, E. Koç, and T. Yavuz. CFD vs. XFOIL of airfoil analysis at low reynolds numbers. *2016 IEEE International Conference on Renewable Energy Research and Applications, ICRERA 2016*, 5:628–632, 2016.

[16] H. HADZIC. *Development and Application of a Finite Volume Method for the Computation of Flows Around Moving Bodies on Unstructured , Overlapping Grids*. PhD thesis, Technischen Universitat Hamburg-Harburg, 2005.

[17] N. J. Higham. *Accuracy and Stability of Numerical Algorithms: Second Edition*. Society for Industrial and Applied Methematics, 2nd edition, 2002.

[18] S. F. Hoerner. *Fluid-dynamic drag: practial informaition on aerodynamic drag and hydrodynamic resistance*. Published by author, 1965.

[19] S. F. Hoerner and H. V. Borst. Fluid-Dynamic Lift: Practical Information on Aerodynamic and Hydrodynamic Lift, 1985.

[20] J. L. V. Ingen. Historical review of work at TU Delft. *38th Fluid Dynamics Conference and Exhibit*, (June):1–49, 2008.

[21] J. John D. Anderson. *Fundamentals of Aerodynamics*. McGraw-Hill, Inc., 2nd edition edition.

[22] J. G. Leishman. *Principles of Helicopter Aerodynamics*. Cambridge Aerospace Series, 2nd edition, 2006.

[23] F. R. Menter. Two-Equation Eddy-Viscosity Turbulence Models for Engineering Applications. *AIAA JOURNAL*, 32(8):1598–1605, 1994.

[24] F. R. Menter, M. Kuntz, and R. Langtry. Ten Years of Industrial Experience with the SST Turbulence Model. *Tubulence, Heat and Mass Transfer 4, Begell House, Inc.*, 2003.

[25] J. Newman. *Marine Hydrodynamics*. The MIT Press, 1977.

[26] B. Pettersen. *Kompendium TMR4247 Marin teknikk 3 Hydrodynamikk*. Kompendieforlaget Akademika forlag, 2007.

[27] R. H. Pletcher, D. A. Anderson, and J. C. Tannehill. *Computational Fluid Mechanics and Heat Transfer*. CRC Press Taylor & Francis Group, 3rd edition, 2013.

[28] J. Rosero, J. Ortega, E. Aldabas, and L. Romeral. Moving towards a more electric aircraft. *IEEE Aerospace and Electronic Systems Magazine*, 22(3):3–9, 2007.

[29] H. Schlichting and K. Gersten. *Boundary- Layer Theory.* Springer-Verlag Berlin Heidelberg 2000, 8th edition, 1955.

[30] Y. T. Shen and R. Epplert. Section Design for Hydrofoil Wings with Flaps, 1979.

[31] W. Shi, M. Atlar, K. Seo, R. Norman, and R. Rosli. Numerical simulation of tidal tubuine based hydrofoil with leading-edge tubercles. *Proceedings of the ASME 2016 35th International Conference on Ocean, Offshore and Arctic Engineering OMAE2016*, 2016.

[32] Simens-STAR-CCM+. Polyhedral mesher. file:///C:/Program%20Files/CD-adapco/12.04.011/STAR-CCM+12.04.011/doc/en/online/index.html#page/STARCCMP%2FGUID-812361C5-EEF9-4028-8A9C-EF5F730917B6%3Den%3D.html.

[33] Simens-STAR-CCM+. Prism layer mesher. file:///C:/Program%20Files/CD-adapco/12.04.011/STAR-CCM+12.04.011/doc/en/online/index.html#page/STARCCMP%2FGUID-4B9B4787-0BEF-4DC6-834D-59346F0C8316%3Den%3D.html.

[34] Simens-STAR-CCM+. Segregated flow model family reference. ffile:///C:/Program%20Files/CD-adapco/12.04.011/STAR-CCM+12.04.011/doc/en/online/index.html#page/STARCCMP%2FGUID-D294DF45-CF81-4A88-AF36-DCA2C36456E5%3Den%3D.html.

[35] Simens-STAR-CCM+. Two dimensional and axisymmetric meshes. file:///C:/ProgramFiles/CD-adapco/12.04.011/STAR-CCM+12.04.011/doc/en/online/index.html#page/STARCCMP%2FGUID-20E3CEAF-B06F-4345-AB4A-51791D55A3FF%3Den%3D.html%23.

[36] Simens-STAR-CCM+. Volume meshers pverview. file:///C:/ProgramFiles/CD-adapco/12.04.011/STAR-CCM+12.04.011/doc/en/online/index.html#page/STARCCMP% 2FGUID-20E3CEAF-B06F-4345-AB4A-51791D55A3FF%3Den%3D.html%23.

[37] S. Steen. *Lecture Notes, TMR4220 Naval Hydrodynamics, Foil and Propeller Theory.* Kompendieforlaget Akademika forlag, 2014.

[38] M. Vinokur. On one-dimensional stretching functions for finite-difference calculations. *Journal of Computational Physics*, 50(2):215–234, may 1983.

[39] F. M. White. *Viscous Fluid Flow.* McGraw-Hill, Inc., 2nd edition, 1991.

[40] T. L. Zhu. A reliability-based safety factor for aircraft composite structures. *Computers and Structures*, 48(4):745–748, 1993.

A   Foil geometries

This appendix presents the two foil geometries analysed in this thesis.
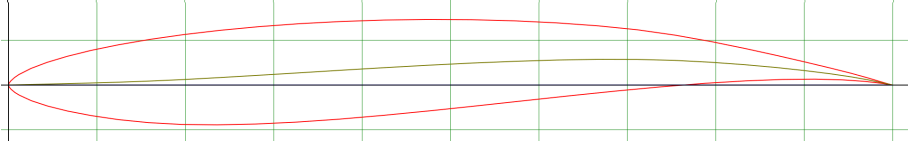

Figure 37: EPPLER E817 hydrofoil profile [2]

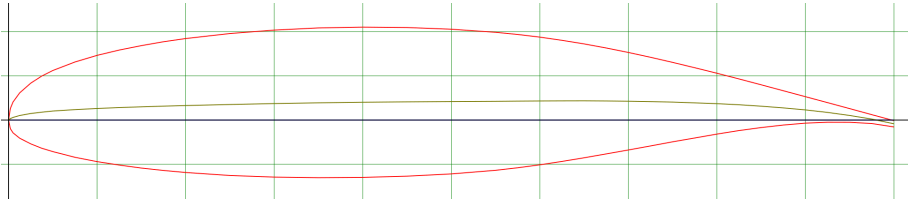Max thickness 11% at 32.9% chord
Max camber 2.9% at 66.7% chord

Figure 38: NASA/LANGLEY LS(1)-0417 (GA(W)-1) airfoil profile [5]

Max thickness 17% at 40% chord
Max camber 2.4% at 65% chord
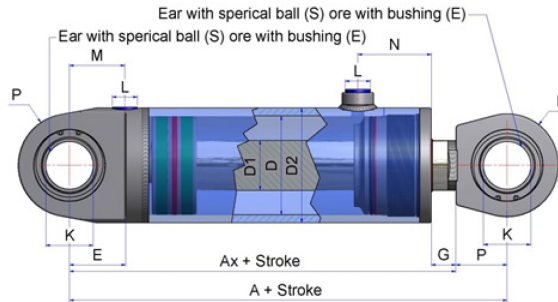
B   Servi CD25 Standard Cylinder

Figure 39: Hydraulic cylinder

Type	Interface	D	A	Ax	D1	D2	E	G	K	L	M	N	P
CD25	S-E/S-E-G-D-F-H	32	163	140	20	40	23	12	20	G 1/4	37	42,5	25
CD25	S-E/S-E-G-D-F-H	40	194	164	25	50	32	10	25	G 3/8	35	53	30
CD25	S-E/S-E-G-D-F-H	50	190	160	25/32	60	32	20	25	G 3/8	26	51	30
CD25	S-E/S-E-G-D-F-H	63	215	180	32/40	73	40	20	30	G 3/8	34	60	35
CD25	S-E/S-E-G-D-F-H	80	240	200	40/50	95	45	25	35	G 1/2	37	64	40
CD25	S-E/S-E-G-D-F-H	90	270	220	45/56	105	50	25	45	G 1/2	48	68	50
CD25	S-E/S-E-G-D-F-H	100	305	252	50/63	120	63	30	50	G 3/4	56	77	53
CD25	S-E/S-E-G-D-F-H	110	320	265	56/70	130	63	30	50	G 3/4	60	85	55
CD25	S-E/S-E-G-D-F-H	125	355	290	63/80	145	71	30	60	G 3/4	70	93	65
CD25	S-E/S-E-G-D-F-H	140	375	302	70/90	165	80	30	70	G 3/4	79	93	73
CD25	S-E/S-E-G-D-F-H	160	420	340	80/100	185	90	35	80	G 1	85	106	80
CD25	S-E/S-E-G-D-F-H	180	440	357	90/110	210	90	35	80	G 1	88	113	83
CD25	S-E/S-E-G-D-F-H	200	470	380	100/125	230	100	35	90	G 1	97	120	90
CD25	S-E/S-E-G-D-F-H	220	620	508	100/140	254	140	40	110	G 1	166	165	112
CD25	S-E/S-E-G-D-F-H	250	675	548	110/160	298	160	40	120	G 1	186	176	127
CD25	S-E/S-E-G-D-F-H	280	745	599	125/180	324	180	40	140	G 1 1/4	210	187	146
CD25	S-E/S-E-G-D-F-H	300	790	636	125/180	343	180	50	140	G 1 1/4	210	200	154
CD25	S-E/S-E-G-D-F-H	320	835	672	140/220	368	200	50	160	G 1 1/4	230	200	163
CD25	S-E/S-E-G-D-F-H	360	900	720	180/220/250	419	215	50	180	G 1 1/4	245	218	180

Figure 40: Hydraulic cylinder dimensions in mm. For full catalogue see www.servi.no[6]